④

AD-A222 822

# David Taylor Research Center

Bethesda, Maryland 20084-5000

A Framework to Correlate a/W Ratio Effects on

Elastic-Plastic Fracture Toughness ($J_c$)

by
R.H. Dodds, Jr.
T.L. Anderson
M.T. Kirk

DTIC

E

DTRC/SME-90/05   A Framework to Correlate a/W Ratio Effects on
Elastic-Plastic Fracture Toughness ($J_c$)

7   095

## MAJOR DTRC TECHNICAL COMPONENTS

CODE 011  DIRECTOR OF TECHNOLOGY, PLANS AND ASSESSMENT

12  SHIP SYSTEMS INTEGRATION DEPARTMENT

14  SHIP ELECTROMAGNETIC SIGNATURES DEPARTMENT

15  SHIP HYDROMECHANICS DEPARTMENT

16  AVIATION DEPARTMENT

17  SHIP STRUCTURES AND PROTECTION DEPARTMENT

18  COMPUTATION, MATHEMATICS & LOGISTICS DEPARTMENT

19  SHIP ACOUSTICS DEPARTMENT

27  PROPULSION AND AUXILIARY SYSTEMS DEPARTMENT

28  SHIP MATERIALS ENGINEERING DEPARTMENT

---

### DTRC ISSUES THREE TYPES OF REPORTS:

1. **DTRC reports, a formal series,** contain information of permanent technical value. They carry a consecutive numerical identification regardless of their classification or the originating department.

2. **Departmental reports, a semiformal series,** contain information of a preliminary, temporary, or proprietary nature or of limited interest or significance. They carry a departmental alphanumerical identification.

3. **Technical memoranda, an informal series,** contain technical documentation of limited use and interest. They are primarily working papers intended for internal use. They carry an identifying number which indicates their type and the numerical code of the originating department. Any distribution outside DTRC must be approved by the head of the originating department on a case-by-case basis.

# REPORT DOCUMENTATION PAGE

| 1a REPORT SECURITY CLASSIFICATION Unclassified | | 1b RESTRICTIVE MARKINGS |
|---|---|---|
| 2a. SECURITY CLASSIFICATION AUTHORITY | | 3 DISTRIBUTION/AVAILABILITY OF REPORT Approved for Public Release; Distribution Unlimited |
| 2b. DECLASSIFICATION/DOWNGRADING SCHEDULE | | |
| 4. PERFORMING ORGANIZATION REPORT NUMBER(S) DTRC/SME-90/05 | | 5 MONITORING ORGANIZATION REPORT NUMBER(S) |

| 6a. NAME OF PERFORMING ORGANIZATION David Taylor Research Center | 6b OFFICE SYMBOL (If applicable) 2814 | 7a. NAME OF MONITORING ORGANIZATION |
|---|---|---|
| 6c. ADDRESS (City, State, and ZIP Code) Bethesda, MD 20084-5000 | | 7b ADDRESS (City, State, and ZIP Code) |

| 8a. NAME OF FUNDING/SPONSORING ORGANIZATION David Taylor Research Center | 8b. OFFICE SYMBOL (If applicable) 011.5 | 9 PROCUREMENT INSTRUMENT IDENTIFICATION NUMBER |
|---|---|---|

| 8c. ADDRESS (City, State, and ZIP Code) Annapolis, MD 21402 | 10 SOURCE OF FUNDING NUMBERS | | | |
|---|---|---|---|---|
| | PROGRAM ELEMENT NO 62234N | PROJECT NO | TASK NO RS345S50 | WORK UNIT ACCESSION NO DN 507603 |

11 TITLE (Include Security Classification)

(U) A Framework to Correlate a/W Ratio Effects on Elastic-Plastic Fracture Toughness ($J_c$)

12 PERSONAL AUTHOR(S)
R.H. Dodds, Jr., T.L. Anderson, M.T. Kirk

| 13a TYPE OF REPORT Research & Develop. | 13b TIME COVERED FROM 2/89 TO 2/90 | 14. DATE OF REPORT (Year, Month, Day) 1990 February | 15 PAGE COUNT 42 |
|---|---|---|---|

16 SUPPLEMENTARY NOTATION
1-2814-950-30, 50FR3/4

| 17 | COSATI CODES | | 18 SUBJECT TERMS (Continue on reverse if necessary and identify by block number) |
|---|---|---|---|
| FIELD | GROUP | SUB-GROUP | Elastic-Plastic Fracture Toughness, Constraint, Shallow Crack, $J$ - |
| | | | |
| | | | |

19 ABSTRACT (Continue on reverse if necessary and identify by block number)

(See Reverse)

| 20 DISTRIBUTION/AVAILABILITY OF ABSTRACT ☐ UNCLASSIFIED/UNLIMITED ☒ SAME AS RPT ☐ DTIC USERS | 21. ABSTRACT SECURITY CLASSIFICATION Unclassified | |
|---|---|---|
| 22a NAME OF RESPONSIBLE INDIVIDUAL M.T. Kirk | 22b TELEPHONE (Include Area Code) 301-267-3755 | 22c OFFICE SYMBOL 2814 |

**DD Form 1473, JUN 86**       Previous editions are obsolete.       SECURITY CLASSIFICATION OF THIS PAGE

Block 19

Single edge–notched bend (SENB) specimens containing shallow cracks ($a/W < 0.2$) are commonly employed for fracture testing of ferritic materials in the lower–transition region where extensive plasticity (but no significant ductile crack growth) precedes unstable fracture. Critical $J$-values ($J_c$) for shallow crack specimens are significantly larger (factor of 2-3) than the $J_c$-values for corresponding deep crack specimens at identical temperatures. The increase of fracture toughness arises from the loss of constraint that occurs when the gross plastic zones of bending impinge on the otherwise autonomous crack–tip plastic zones. Consequently, SENB specimens with small and large $a/W$ ratios loaded to the same $J$-value have markedly different crack–tip stresses under large–scale plasticity. Detailed, plane–strain finite–element analyses and a local stress–based criterion for cleavage fracture are combined to establish specimen size requirements (deformation limits) for testing in the transition region which assure a single parameter ($J$) characterization of the crack–tip stress field. Moreover, these analyses provide the first quantitative framework to correlate $J_c$-values with $a/W$ ratio once the deformation limits are exceeded. The new procedures are directly applicable to estimate the toughness values for shallow crack specimens from results of tests performed on conventional deep–crack specimens. The increased toughness values for shallow–crack specimens are required to perform realistic assessments of the surface–breaking defects most commonly encountered in structures. The correlation procedure is applied to an extensive set of test results for an A36 steel and is shown to successfully correlate the $a/W$ ratio effects on the measured fracture toughness values in the transition range.

# TABLE OF CONTENTS

# LIST OF FIGURES

Figure 11: Relationship between the normalized $J$–integral values in SENB specimens with those of SSY conditions which generate equivalent opening mode stresses at $r = 4\delta_t$ ahead of the crack tip for hardening exponent $n = 10$.

Figure 12: Relationship between the normalized $J$–integral values in SENB specimens with those of SSY conditions which generate equivalent opening mode stresses at $r = 4\delta_t$ ahead of the crack tip for hardening exponent $n = 50$.

Figure 13: Experimentally determined critical $J$–values for an A36 steel showing the estimated lower–bound curves for $a/W = 0.15$ generated from the $a/W = 0.5$ curve using the constraint loss correction procedure.

Figure 14: Comparison of experimentally determined critical $J$–values for an A36 steel with data values corrected for constraint loss.

Figure 15: Comparison of crack opening stress through the thickness of a deeply notched SENB specimen relative to centerplane values. Distances ahead of crack front are $2$–$4\delta_t$.

Figure 16: Ratio of $J$–values in deeply notched, SENB specimens to $J$–values in small–scale yielding that generate the same crack opening stresses for increased levels of applied loading and hardening exponents $n = 5$, $10$, and $50$. Proposed size requirement for $J_c$ testing to assure geometry independent toughness measures and current size requirement for $J_{Ic}$ are indicated.

# LIST OF TABLES

Table 1: Constraint factors $m$ for $J$–CTOD relationships.

# EXECUTIVE SUMMARY

This study provides the first quantitative step toward development of a framework to address the issue of constraint that severely hampers the assessment of shallow, surface-breaking defects. Realistic assessments require that crack-tip conditions (i.e. stress and strain) in simple laboratory test specimens closely match those at the defect in a structural component. When similar crack-tip conditions prevail, critical values of macroscopic toughness (J) measured in the test specimen are directly applicable to assess the criticality of the structural defect. However, large-scale plastic deformation and effects of geometry lead to complex relationships between J and stress-strains at the crack-tip that are not currently understood.

Fracture toughness values obtained from extensive testing of shallow-notch bend specimens have been shown previously to correlate qualitatively with the fracture of specimens containing shallow, surface defects. The absence of a quantitative understanding for this behavior motivated the current study. The effects of in-plane plastic flow on constraint for through-cracks in bend-bars are essentially resolved in the present work through careful numerical analyses and consideration of a single fracture mode (stress-controlled). Quantitative guidelines to estimate fracture toughness values for any a/W ratio given test results at one a/W ratio, generally 0.5, are an immediate benefit of these numerical computations. Moreover, the procedure developed here to quantify in-plane constraint appears equally promising to quantify thickness effects for through-cracks in bend bars which leads directly to the surface crack configuration of most practical interest.

# ABSTRACT

Single edge-notched bend (SENB) specimens containing shallow cracks ($a/W < 0.2$) are commonly employed for fracture testing of ferritic materials in the lower-transition region where extensive plasticity (but no significant ductile crack growth) precedes unstable fracture. Critical $J$-values ($J_c$) for shallow crack specimens are significantly larger (factor of 2-3) than the $J_c$-values for corresponding deep crack specimens at identical temperatures. The increase of fracture toughness arises from the loss of constraint that occurs when the gross plastic zones of bending impinge on the otherwise autonomous crack-tip plastic zones. Consequently, SENB specimens with small and large $a/W$ ratios loaded to the same $J$-value have markedly different crack-tip stresses under large-scale plasticity. Detailed, plane-strain finite-element analyses and a local stress-based criterion for cleavage fracture are combined to establish specimen size requirements (deformation limits) for testing in the transition region which assure a single parameter ($J$) characterization of the crack-tip stress field. Moreover, these analyses provide the first quantitative framework to correlate $J_c$-values with $a/W$ ratio once the deformation limits are exceeded. The new procedures are directly applicable to estimate the toughness values for shallow crack specimens from results of tests performed on conventional deep-crack specimens. The increased toughness values for shallow-crack specimens are required to perform realistic assessments of the surface-breaking defects most commonly encountered in structures. The correlation procedure is applied to an extensive set of test results for an A36 steel and is shown to successfully correlate the $a/W$ ratio effects on the measured fracture toughness values in the transition range.

# ADMINISTRATIVE INFORMATION

# INTRODUCTION

Single edge–notched bend (SENB) specimens containing shallow, through cracks ($a/W < 0.2$) are commonly employed for fracture toughness testing in the ductile–to–brittle transition region of ferritic materials. The testing of particular microstructures in weldments frequently dictates the use of shallow crack specimens when deeply cracked specimens are impossible to obtain due to material thickness and weld orientation. Shallow crack specimens also provide an opportunity to better match the crack–tip conditions in a structural component containing, for example, a surface flaw loaded primarily in tension. Fracture toughness values obtained from deeply notched bend specimens characterize microstructures and constraint conditions rarely experienced by in–service structures, making such specimens inappropriate for use in assessments of structural integrity.

Recent experimental studies [1-9] have demonstrated a significant increase in the apparent elastic–plastic fracture toughness, characterized by the $J$–integral [10], for specimens with shallow cracks when tested in the transition region. Figure 1 illustrates the differences in toughness–temperature relationships typical of a mild structural steel tested with deep ($a/W \approx 0.5$) and shallow ($a/W \approx 0.15$) crack specimens. Load–displacement records for specimens tested throughout the transition region show some degree of non-linearity; plastic hinges commonly form prior to failure even towards the lower–end of the transition region. At upper–shelf temperatures, ductile fracture initiation by microvoid coalescence and shear localization is generally linked to the achieving of a critical strain over an intensely deformed process zone at the blunted crack tip [11]. Conversely, at or near the lower–shelf temperatures, brittle (unstable) fracture initiation by cleavage is attributed to achieving a critical tensile stress over a significant microstructural distance [12,13]. The initiation of stress–controlled cleavage fracture in an SENB specimen depends upon material properties (cleavage fracture stress, flow characteristics) and structural parameters which govern crack–tip conditions ($a/W$ ratio, specimen thickness). Assessments of structural integrity generally focus on the cleavage fracture mechanism due to the possibility of a local crack–tip instability triggering a catastrophic structural failure.

In the lower–transition region, unstable fractures with cleavage as the microstructural separation process occur following plastic deformation that exceeds $K_{Ic}$ validity limits (ASTM E399–83) but without significant ductile tearing. The onset of stable, ductile tearing represented by $J_{Ic}$ (ASTM E813–87) defines the upper–transition region, although unstable fractures triggered by cleavage are sometimes observed after ductile tearing. Critical $J$–values for cleavage fracture toughness in the lower–transition region are denoted $J_c$ to differentiate from the larger values ($J_{Ic}$) that apply to the onset of ductile tearing. As shown in Figure 1, $J_c$–values for short crack specimens may be significantly larger than values for deep crack specimens at identical temperatures in the lower–transition region. The increased ductility of shallow crack specimens also lowers the transition temperature and increases the ductile initiation toughness, $J_{Ic}$ [1,6-8].

2

The increase of $J_c$-values in shallow notch specimens develops when the in-plane plastic deformation of the gross bending impinges on the local crack-tip fields which relaxes the kinematic constraint against further plastic flow. The joining of crack-tip plastic zones with those at the tension surface for shallow notches sharply reduces the stress triaxiality (see Fig. 1). Deeply notched specimens of very low hardening materials also exhibit a loss of crack-tip constraint, but not as severe as for shallow notches. Once the global and local plastic fields interact, the crack-tip strains and stresses no longer increase in proportion to one another according to the asymptotic singular fields derived by Hutchinson [14] Rice and Rosengren [15] (HRR) which have amplitudes uniquely governed by the single parameter $J$. The shallow crack specimens exhibit smaller stresses and larger strains than those represented by the highly constrained HRR fields. Thus deep and shallow notched specimens loaded to the same applied $J$-value (that produces significant plasticity) exhibit very different stress fields at the crack-tip which leads to the specimen size dependence of critical $J_c$-values. However, $J$ retains usefulness as a macroscopic measure of fracture toughness, albeit geometry and material dependent, to link the crack-tip stress-strain fields with imposed loading even though strict coupling with the HRR fields no longer holds.

McMeeking and Parks [16], Shih and German [17], and Shih [18] performed plane strain finite-element analyses for deeply notched SENB specimens to establish the levels of plastic deformation beyond which the single parameter HRR fields no longer dominate or characterize the complete crack-tip conditions. The requirement may be stated as

$$ b \geq \frac{\mu_{cr} J_{Ic}}{\sigma_{flow}}; \quad \mu_{cr} = 25 \text{ for } a/W \geq 0.5 \tag{1} $$

where b is the uncracked ligament length (W–a) and $\sigma_{flow}$ is the material flow stress, defined as the average of the yield and tensile strength. Generally, this limit is satisfied at deformations well into the large-scale yielding range represented by the formation of a plastic hinge. To establish the value for $\mu_{cr}$, general agreement ($\approx 10\%$) between the finite-element and HRR crack-tip fields was sought over a distance of 3–5 $\delta_t$, where $\delta_t$ denotes the crack tip opening displacement (CTOD). No explicit consideration was given of a fracture separation process in assigning a value for $\mu_{cr}$, although the intended use was for $J_{Ic}$ testing. Parks [19,20] notes the inherent difficulty of such approaches to establish limits assuring $J$-dominance because the stress fields change gradually from the $J$-dominated ones as loading is increased; assigning values for $\mu_{cr}$ thus introduces subjective judgements. Nevertheless, Eq (1) has proven adequate to guarantee nearly size-independent $J_{Ic}$ values for initiation of ductile tearing and is incorporated in the ASTM E813–87 test procedure. However, this requirement is now believed too lenient for unstable fractures resulting from stress-controlled cleavage because even a slight reduction of crack-tip stresses below the HRR values can produce a significant elevation of the critical $J$-value [21–23].

The present work focuses on quantifying specimen size effects for unstable fracture by cleavage when plastic deformation exceeds the customary $K_{Ic}$ validity limits. Very detailed finite-element analyses along the lines of those in [17,18] are generated for both shallow and deep notch bend specimens for a wide range of strain-hardening behavior. The finite-element models fully resolve crack-tip stress fields over the length scale of $3-10\delta_t$ for the full range of loading. A microscopic, stress-based criterion for cleavage fracture is adopted to establish specimen size requirements (deformation limits) which assure unique characterization by a macroscopic parameter ($J$) at failure. The recommended size requirements are significantly less stringent than those of E399-83 but more restrictive than the E813-87 requirements of Eq. (1). Moreover, by requiring identical values of the microscopic criterion at failure, the finite-element analyses provide a framework to correlate $J_c$-values with $a/W$ ratio once the deformation limits are exceeded (the micromechanism of failure is assumed to remain cleavage). The correlation procedure is shown to successfully remove the geometry dependence of fracture toughness values in the lower-transition range for an A36 steel.

## STRESS FIELDS FOR ANALYSIS OF CLEAVAGE FRACTURE

A study of specimen size effects on cleavage fracture toughness must correlate the various crack-tip stress fields over the potential fracture process zone. The plane-strain HRR fields provide the starting point for such comparisons and are given by,

$$\sigma_{ij}(r,\theta) \to \sigma_o \cdot \left[ \frac{J}{\alpha \epsilon_o \sigma_o I_n r} \right]^{\frac{1}{n+1}} \cdot \tilde{\sigma}_{ij}(\theta,n) \equiv \sigma_{ij}^{HRR} \tag{2a}$$

$$\epsilon_{ij}(r,\theta) \to \epsilon_o \cdot \left[ \frac{J}{\alpha \epsilon_o \sigma_o I_n r} \right]^{\frac{n}{n+1}} \cdot \tilde{\epsilon}_{ij}(\theta,n) \equiv \epsilon_{ij}^{HRR} \tag{2b}$$

where $r$ and $\theta$ are the polar coordinates centered on the crack tip, $I_n$ is an integration constant (function of $n$ only), and $\tilde{\sigma}_{ij}$ and $\tilde{\epsilon}_{ij}$ are dimensionless functions. Tables of the HRR functions are provided in [24]. The material follows a pure power-law constitutive model which in uniaxial form is

$$\epsilon/\epsilon_o = \alpha(\sigma/\sigma_o)^n \tag{3}$$

where $\sigma_o$ an effective yield stress, $\epsilon_o = \sigma_o/E$ is the reference (yield) strain; $\alpha$ is a dimensionless factor and $n$ is the strain hardening exponent. Generalization of this relation to multiaxial states using deformation ($J_2$) plasticity yields strain components of the form

$$\frac{\epsilon_{ij}}{\epsilon_o} = \alpha \frac{3}{2}(\sigma_e/\sigma_o)^{n-1} \frac{s_{ij}}{\sigma_o} , \qquad \sigma_e = (\frac{3}{2}s_{ij}s_{ij})^{\frac{1}{2}} \tag{4}$$

where $s_{ij}$ is the stress deviator and $\sigma_e$ is the Mises equivalent tensile stress.

Eqs. (2-4) provide the asymptotic, small-strain theory results for an ideally sharp crack-tip under monotonically increasing, Mode I loading. These fields are not applicable

4

within the finitely deformed blunting zone which evolves at the crack-tip. The crack-tip opening displacement, $\delta_t$, provides a convenient length scale to describe near-tip distances, such as the blunting zone size. Shih [25] defined $\delta_t$ as the separation where $\pm 45°$ lines emanating from the crack tip intercept the opening faces. For the HRR displacement fields, the form of $\delta_t$ is

$$\delta_t = d_n(a\epsilon_o, n) \cdot J/\sigma_o \tag{5}$$

where the coefficient $d_n$ is weakly dependent on $a\epsilon_o$ and varies from 0.3 for small $n$ to 0.8 for large $n$.

The length scale over which the single-term fields in Eqs. (2) adequately describe the response at finite distances from the crack tip is obtained through consideration of the boundary-layer problem referred to as small-scale yielding (SSY). Originally proposed by Rice and Tracey [26], McMeeking [27] and recently used by Parks and Wang [19], the SSY model consists of an annular region containing a sharp crack tip which is subjected to increasing displacements of the elastic (Mode I) singular field on the outer circular boundary. Steady state conditions develop in which strains and stresses at all angles scale with $r/(J/\sigma_o)$ and $r/\delta_t$, as do the HRR fields, and persist under increasing deformation until the plastic zone senses the circular boundary. Finite-element analyses for the SSY problem indicate divergence of the HRR and SSY fields for $r > 2\text{-}3\,\delta_t$, with smaller stresses and larger strains predicted by the SSY model. Thus, Eqs. (2) may be considered the leading term of the complete near-tip fields provided by the SSY model.

Finite deformation (blunting) analyses for the SSY model and for deeply notched bend-bar models by McMeeking [27] and McMeeking and Parks [16] predict the location of maximum tensile stress on $\theta = 0$ at approximately $2\text{-}4\,\delta_t$ ahead of the blunted tip. Opening stresses nearer to the crack tip are relaxed by a loss of triaxiality due to the free surface of the blunted tip. The fracture process zone for cleavage thus lies beyond the finitely deformed zone adjacent to the blunted tip and beyond the region over which the asymptotic HRR field is adequate to describe the stress magnitudes. Moreover, differences in stresses for the SSY model predicted by the notch-blunting analyses and by the small-strain analyses (with a sharp crack) become insignificant for $r > 2\text{-}3\,\delta_t$. These observations suggest that detailed finite-element solutions for SENB specimens based on small-strain theory are valid to assess fields ahead of the crack tip when stress-controlled cleavage is the fracture separation process of interest. Finite-element meshes must fully resolve the stress fields over a length-scale of $2\text{-}10\,\delta_t$ for the levels of loading examined. To assess effects of specimen size, the SENB stresses over this region should be compared to those of the SSY model rather than HRR.

With the basis for comparison of crack-tip stress fields established, a simple microscopic model for cleavage initiation is adopted. Unstable fracture is defined to occur when the tensile stress on the crack plane at $r = 4\delta_t$ reaches a critical value. In subsequent sections, the particular choice of 4, 5, or $6\,\delta_t$ is shown to be insignificant as the stress fields

5

scale identically with macroscopic loading parameters ($J$, $\delta_t$) over this region. Preliminary studies [28] of alternative criterion that consider the statistical nature of cleavage initiation and the volume of the process zone support the use of a simple, single-point comparison for the present assessment of size effects.

For a specified material, the microscopic failure criterion is related to applied $J$-values in SENB specimens through the procedure illustrated in Fig. 2. $J$-values for SENB specimens ($J_{SENB}$) are plotted against $J$-values for the SSY model ($J_{SSY}$) that impose the identical opening mode stress at $r = 4\delta_t$ on the crack plane. Thus, when $J_{SENB} = J_{SSY}$ the crack-tip stresses match those for an infinite body; fracture toughness values obtained in SENB specimens under such conditions are geometry independent. However, large-scale plasticity and size effects require significant increases in $J_{SENB}$ relative to $J_{SSY}$ to maintain identical crack-tip stresses as indicated in Fig. 2. When generated for specific material properties and specimen sizes, results of the form shown in Fig. 2 may be used to scale fracture toughness data to account for the $a/W$ ratio by indexing a given $J_c$ for one $a/W$ through the $J_{SSY}$ to obtain $J_c$ for a different $a/W$. The applications are two-fold: 1) the geometry dependence of fracture toughness data for different $a/W$ ratios may be eliminated through correlations to a single $a/W$ ratio or to the SSY model, and 2) commonly available test results for deep notch specimens ma·· be appropriately scaled for fracture assessments of shallow notched structures.

## NUMERICAL PROCEDURES

Plane-strain finite element analyses were conducted to obtain very detailed resolutions of the crack-tip stress fields for the SSY model and for SENB specimens. The numerical models employ conventional small-strain theory and address a wide range of material strain hardening. The remainder of this section outlines the details of the models and solution procedures, beginning with those aspects common to both the SSY and SENB analyses.

### CONSTITUTIVE MODEL

The material model employs $J_2$ deformation plasticity theory (nonlinear elasticity). The uniaxial stress-strain curve follows the Ramberg-Osgood form of Eq. (3) with an additional term linearly dependent on stress, thus

$$\epsilon/\epsilon_o = \sigma/\sigma_o + a(\sigma/\sigma_o)^n \tag{6}$$

The total strain components are related to the total stresses by Eq. (4) with the addition of deviatoric and volumetric terms that vary linearly with stress according to Eq. (6),

$$\epsilon_{ij} = [\frac{1 + \nu}{E} + \frac{3a\epsilon_o}{2\sigma_o}(\sigma_e/\sigma_o)^{n-1}]s_{ij} + \frac{1 - 2\nu}{3E}\sigma_{kk}\delta_{ij} \tag{7}$$

where is the $\sigma_{kk}$ is the trace of the stress tensor and $\delta_{ij}$ is the Kronecker delta. Details of the numerical implementation follow those described by de Lorenzi and Shih [29].

The finite-element analyses for each configuration are repeated for three levels of strain hardening, high ($n = 5$), moderate ($n = 10$), and very low ($n = 50$). The parameter $a$ is assigned a value of 1. Other properties typical of those for a moderate strength structural steel are adopted in the computations, $\epsilon_o = 0.002$, $\sigma_o = 60$ ksi (414 MPa) and Poisson's ratio, $v = 0.3$; in this case $\sigma_o$ corresponds to the 0.2% offset yield strength, $\sigma_{YS}$. Figure 3 illustrates the relative degrees of hardening represented by the selected exponents.

## FINITE ELEMENTS AND CRACK-TIP MODELS

Eight-noded isoparametric elements with reduced (2x2) Gauss quadrature are employed in all of the models. Reduced integration eliminates locking of arbitrarily shaped elements once the incompressible conditions of fully plastic deformation constrain volumetric changes in the displacement gradients [30].

Concentric rings of polygonal-shaped elements surround the crack-tips. The innermost ring contains elements collapsed into wedge shapes with side nodes retained at the mid-point position. Initially coincident nodes at the crack tip are unconstrained. This model produces a $1/r$ strain singularity appropriate for $n \rightarrow \infty$ and allows blunting deformations of the tip.

Preliminary analyses of all configurations and hardening exponents were conducted using coarse meshes to obtain the range of crack-tip opening displacements present at large-scale yielding. The final meshes were then constructed to have concentric rings of elements enclosing the crack tip with sizes that increase geometrically with $r$. The mesh gradation provides at least 8–10 elements over the domain $2\delta_t < r < 10\delta_t$ except for the very earliest stages of loading when $\delta_t$ is truly infinitesimal.

Stresses are computed at the 2x2 Gauss point locations with nodal stresses obtained by a least-squares extrapolation of the Gauss point values [31]. Extrapolated nodal values are then arithmetically averaged without regard to sizes of elements incident on the nodes. Comparisons of opening mode stresses, $\sigma_{yy}$, along $\theta = 0$ for the various configurations utilize the averaged stresses of corner nodes. Mesh sensitivity studies demonstrated the adequacy of this procedure.

Crack tip opening displacements in the finite element models are determined by applying the $\pm 45°$ intercept procedure to the blunted crack tips.

## SMALL-SCALE YIELD (SSY) MODELS

Figure 4 shows the element mesh defined for the circular domain of radius $R$ that contains a sharp crack with tip located at $r = 0$. Symmetrical boundary conditions are applied on the crack plane ($X \geq 0$, $Y = 0$). Loading of the model is accomplished by imposing displacement increments of the elastic singular field for Mode I on the outer circular boundary:

$$\Delta u(r, \theta) = \frac{(1 + v)\Delta K_I}{E}(\frac{r}{2\pi})^{\frac{1}{2}}(3 - 4v - cos\theta)\ cos(\theta/2) \tag{8a}$$

$$\Delta v(r, \theta) = \frac{(1 + v)\Delta K_I}{E} (\frac{r}{2\pi})^{\frac{1}{2}}(3 - 4v - \cos\theta) \; \sin(\theta/2) \tag{8b}$$

$K_I$ is increased until the plastic zone reaches $\approx R/10$–$R/15$ at which point the computed $J$ is slightly smaller than $K_I^2(1 - v^2)/E$.

The mesh contains 2277 nodes and 720 elements divided into 40 rings of 18 equally sized fans. Element sizes decrease geometrically as $r \to 0$ to focus the greatest refinement near the crack tip. Analyses with additional mesh refinement did not alter the predicted stresses over the crack plane.

## SENB MODELS

Three $a/W$ ratios are considered: 0.05, 0.15, and 0.50. The finite–element model defined for the three–point bend specimen with $a/W = 0.15$ is shown in Fig 5. Conventional plan-form dimensions are employed, span $S = 4W$, with $W = 2$ in. (5.08 cm) used in the numerical solutions. Symmetry conditions permit modeling of only one–half of the specimen. The half–symmetric mesh contains 350 elements and 1200 nodes; very similar mesh densities are defined for $a/W = 0.5$, 0.05. The core of 240 elements for the crack–tip region is common for all three meshes. The core elements are divided into 30 rings of increasing size with 8 equally spaced, $\Delta\theta$, elements per ring. Elements incident on the crack tip have side length $L = 0.0002$ in. (0.005 mm). The much greater refinement in $r$ relative to $\theta$ is necessary to provide 8–10 elements over the region $2\delta_t < r < 10\delta_t$ at low–to–moderate loading levels.

The mid–span load is distributed over two small elements to minimize effects of the local singularity of an idealized point load.

## SOLUTION PROCEDURES

Loads are increased to final values in variably sized increments, typically 20–40 steps, with full Newton iterations performed within each increment to remove residual forces. Very stringent criterion are defined which ensure convergence of strains and stresses in the third significant figure. Three to five iterations are generally required for convergence with the larger number of iterations and load steps needed for very low hardening ($n = 50$). Given the strain path independence of stresses in deformation plasticity, converged values for strains and stresses are invariant of the load step sizes used in the computations. The number and magnitude of the load steps is selected to provide a complete description of the response history and to maintain quadratic convergence of the Newton iterations.

$J$–integral values are obtained using the domain integral method [32,33]. The variation among $J$–values computed over element rings adjacent to the crack tip elements and rings remote from the tip is less than 1% as expected for the very refined models and deformation plasticity.

Numerical computations were performed on Apollo workstations using PATRAN [34] for mesh generation and POLO–FINITE [35] for analyses and domain integral computations.

# COMPUTATIONAL RESULTS

## SSY MODELS

The SSY models provide the tensile stress distributions on the crack plane for comparison and normalization of the SENB results. In nondimensional form, Figure 6 compares the finite–element SSY results for $n = 10$ with the HRR values given by Eqs. (2). SSY results are shown for two levels of applied loading that produce plastic zones with sizes $r_p/R = 1/35$ and $1/10$. For the larger plastic zone, $K_I$ computed from the domain integral $J$–value using the elastic conversion differs less that 2% from the $K_I$ imposed through displacements on the circular boundary. The SSY stresses possess similarity length scales $r\sigma_o/J$, $r/\delta_t$ and reveal a slowly growing divergence from the HRR stresses. At $r = 4\,\delta_t$ the SSY stress for $n = 10$, for example, has decreased to 90% of the HRR value. Similar plots constructed for $n = 5, 50$ and for other angular orientations display equal scalability of the SSY stresses with $r\sigma_o/J$ and $r/\delta_t$.

Normalizations of the SENB fields require the SSY stress for arbitrary, nondimensional positions along $\theta = 0$. For convenience, continuous functions are constructed to fit the finite–element nodal values of SSY stress which take the form:

$$\sigma_{yy} = \sigma_o a \beta^b e^{c\beta} \tag{9a}$$

where

$$\beta = r/(J/a\sigma_o\epsilon_o) \tag{9b}$$

and $a$, $b$, and $c$ are curve fitting parameters. This functional representation is adopted strictly to minimize errors in curve fitting; no attempt is made to enforce the HRR field for $r/(Ja\sigma_o\epsilon_o) < 0.0005$ where finite–element stresses may be less reliable. The table included in Fig. 6 provides the curve fitting parameters for each strain–hardening exponent.

## SENB SPECIMENS

Figures 7–11 provide the essential results of the finite–element analyses needed to correlate local stress fields for the different $a/W$ ratios. At increasing levels of applied load, Fig. 7 shows the variation of stress component $\sigma_{yy}$ directly ahead of crack tip for $a/W = 0.15$ and $n = 10$. The SENB results are normalized by stresses of the SSY model when loaded to the same $J$–value. The normalized stresses are plotted against distance ahead of the crack–tip measured in multiples of $\delta_t$. Points that would lie within the blunting zone of a finite–deformation analysis, $r < 2$–$3\,\delta_t$, are not shown. The intensity of deformation for each curve

9

is indicated through a reference limit load, $P_o$, defined for a perfectly plastic material of yield stress $\sigma_o$ [9,36] and through the magnitude of CTOD relative to the crack length.

Figure 7 shows that the SENB stresses steadily decrease below the SSY values for increasing load. Very similar responses are obtained for the other hardening exponents and $a/W$ ratios. Agreement between SENB and SSY stresses increases with greater degrees of strain hardening and larger $a/W$ ratios, i.e., $a/W = 0.5$ with $n = 5$ provides the closest agreement with the SSY solution over the complete range of loading. The relative "flatness" of the curves for $P/P_o < \approx 1$ indicates that SENB stresses ahead of the crack-tip have the same spatial variation as the SSY stresses when distances are normalized by $r/\delta_t$ or $r/(J/\sigma_o)$. Amplitudes of the SENB stresses, however, are substantially lower than SSY values at the same applied $J$.

The similarity in the spatial variation of the SENB and SSY stresses also applies along other rays of constant $\theta$. Figure 8 compares nondimensional contours of principal stress for the SSY solution with those for an SENB specimen of $a/W = 0.5$ at a low level of loading. Both the shape *and* amplitude of the contours coincide except for the small spike at $\pm 45°$ which is attributed to the coarser mesh in the angular direction for the SENB models (the element mesh for the SSY model has twice the angular refinement of the SENB mesh). The areas enclosed by the SSY and SENB contours in Fig. 8 agree to within 3%. Figure 9 illustrates the effects of large-scale yielding on nondimensional contours of principal stress for $n = 10$ and $a/W = 0.05, 0.5$. Although the contours for both cases maintain the constant shape of SSY, their size (when normalized by $J$) decreases with increased loading and extent of plastic deformation. The absolute size of the contour actually increases with $J$, but at a slower rate than predicted by the SSY field, even for the highly constrained $a/W = 0.5$ geometry.

Figures 7-9 provide two key results. First, Fig. 7 clearly indicates that for each load level a *constant* scaling factor is applicable to correlate the SENB and SSY stresses at least over the length-scale of 4-8 $\delta_t$. The scaling factor is defined by the ratio of $J_{SENB}/J_{SSY}$ necessary to bring the SENB stresses into agreement with the SSY stresses over this region. Since a critical value for $J_{SSY}$ represents a size-independent cleavage fracture toughness, the $J_{SENB}/J_{SSY}$ ratio quantifies the geometry dependence of $J_c$, the measured fracture toughness of a finite-size specimen. For deeply notched specimens with moderate to high hardening, $J_{SENB}/J_{SSY}$ approaches unity for $a\sigma_o/J$ greater than $\approx 200$. For shallower cracks and light hardening, this ratio exceeds 3-4, i.e., for a given $J_{SSY}$, significantly larger $J$-values are needed in shallow notched SENB specimens to generate equivalent SSY stresses.

The second key result of Figs. 7-9 is the insensitivity of the distance ahead of the crack tip and angle $\theta$ at which SENB and SSY stresses are equated to define the $J_{SENB}/J_{SSY}$ ratio. The simple procedure adopted for the present study enforces equality of $\sigma_{yy}$ stresses at $r = 4 \delta_t$ on $\theta = 0$ to define the $J_{SENB}/J_{SSY}$ ratio. The more elaborate scheme which equates

areas enclosed by principal stress contours to define the $J_{SENB}/J_{SSY}$ ratio predicts essentially identical scaling factors [28].

Figures 10-12 present the effects of $a/W$ and hardening exponent on the $J_{SENB}/J_{SSY}$ ratio. Figure 2 represents the conceptual form for these results and illustrates their use to correlate toughness values between $a/W$ ratios. The data in Figs. 10-12 are presented as the *effective* driving force for cleavage, $J_{SSY}$ plotted against the apparent (measured) driving force, $J_{SENB}$. The dashed line on each figure represents the small-scale yielding limit, where $J_{SENB} = J_{SSY}$ by definition. The $J$-values are normalized with the remaining ligament length, $b$, rather than crack length simply to better separate the curves. The flow stress, rather than $\sigma_o$, is also used to normalize $J$ to make the results readily applicable to other than power-law hardening materials. The flow stress for a Ramberg-Osgood material is estimated with the following relationship:

$$\sigma_{flow} = \frac{\sigma_o}{2}[1 + \frac{(N/\epsilon_o)^N}{exp(N)}] \tag{10}$$

where $N = 1/n$. Equation (10) is derived by solving for the tensile instability point in Eq. (6), converting true-stress to engineering stress, and averaging $\sigma_o$ and the estimated tensile strength.

Note that scales on the figures are different to accommodate the full extent of loading in each case. The curves in Figs. 10-12 all agree with the SSY limit at low $J$-values but show significant deviation as $J$ increases. The divergence from SSY occurs more rapidly and at lower $J$-values in the shallow notched specimens and in low hardening materials. For $n = 50$ (Fig. 12), the effective driving force saturates at a constant value, particularly so for $a/W = 0.5$; further increases of $J$ do not affect $J_{SSY}$. Once a specimen reaches the saturation value of $J_{SSY}$, stresses ahead of the crack-tip no longer increase and the likelihood of cleavage fracture with further loading decreases considerably. Cleavage in such cases would seem probable only if the crack grew by ductile tearing and sampled a microstructurally weak feature. The procedure to correlate toughness values between $a/W$ ratios and to SSY conditions is graphically illustrated in Fig. 2.

## APPLICATION TO EXPERIMENTAL DATA

With the aid of Figs. 10-12, experimental values of cleavage fracture toughness may be corrected (or scaled) to account for the loss of constraint due to large-scale (in-plane) yielding. Given the measured toughness ($J_c$), specimen size, $a/W$ ratio, and material hardening characteristics, the equivalent toughness ($J_{SSY}$) for an infinite size specimen can be estimated. Alternatively, the critical $J$ for one $a/W$, for example 0.15, can be estimated from the measured $J_c$ for another $a/W$, e.g., 0.5. Both procedures are applied here to the extensive set of fracture toughness data for A36 steel recently reported by Sorem, et al. [1].

Sorem tested SENB specimens having a square section (B x B) with thickness of 31.8 mm (1.25 in.) for the A36 material. Full transition curves were generated for $a/W$ ratios of

0.15 and 0.5. In addition, three–dimensional, finite–element analyses were performed to support the conversion of measured loads, load–line displacements and crack mouth opening displacements into applied $J$–values without assumptions on the location of rotation points, $\eta$–factors, etc. The uniaxial stress–strain curve for the A36 material exhibits a well–defined yield plateau followed by relatively high strain hardening. The power–law behavior of the Ramberg–Osgood model in Eq. (6) is reasonably followed in the strain–hardening region. The hardening exponent, $n$, for this material is estimated to be 6.

Figure 13 shows $J_c$ test results for the A36 steel; values for individual specimens are plotted for $a/W = 0.15$ while only the lower–bound curve is shown for $a/W = 0.5$. At –43°C and below, all but one of the $a/W = 0.15$ specimens failed by cleavage without significant stable crack extension. A fibrous thumbnail denotes evidence of ductile tearing prior to unstable fracture. The shallow notch specimens show a significant increase in the apparent fracture toughness throughout the transition region. $J_c$ values for $a/W = 0.5$ represented by the lower–bound curve are corrected for constraint loss, using Figs. 10 and 11, to predict a corresponding lower–bound curve for $a/W = 0.15$ using $n = 5,10$ hardening exponents. Figure 13 shows that the lower–bound curve predicted for $n = 5$ slightly under estimates the correction needed for constraint loss while the $n = 10$ curve over corrects.

The typical scatter in toughness values shown for the $a/W = 0.15$ specimens tested at –43°C and –76°C suggests that each test result at a specified temperature should be corrected individually for constraint loss. The crack–tip stress fields differ significantly at failure due to the plastic deformation for the minimum and maximum toughness values, particularly at –43°C. Consequently, the largest correction for constraint loss should be applied to the specimen failing with the maximum toughness; similarly, the specimen failing with the lowest toughness requires the least correction. Figures 10 and 11 are used again to obtain factors that convert the measured toughness of each test specimen (deep and shallow notch) to a constraint corrected SSY value. Linear interpolation between $n = 5$ and $n = 10$ is applied to obtain the factors for $n = 6$ corresponding to the A36 steel. Figure 14 shows all the measured toughness values for these two temperatures and $a/W$ ratios along with the corrected small–scale yielding values ($J_{SSY}$) for each data point. The values of toughness corrected for constraint loss at each temperature agree very well; differences in "corrected" toughnesses for the two temperatures reflect the real differences in the toughness property of the material. Moreover, the corrected values have less scatter than the uncorrected data. The decreased scatter reduces the number of specimens that must be tested to establish specific confidence limits on lower–bound values. Anderson and Dodds [28] provide a complete statistical analysis of the A36 data and the effects of the constraint correction procedure.

## CONSTRAINT LOSS CORRECTIONS FOR CTOD

Figures 10–12 provide the correction factors for constraint loss in terms of the $J$–integral. Corresponding figures may be constructed with CTOD ($\delta_t$) rather than $J$ as the fracture

characterizing parameter. The HRR relationship between $J$ and $\delta_t$ defined in Eq. (5) is generalized using the material flow stress into the form

$$J = m\sigma_{flow}\delta_t \tag{11}$$

where the coefficient $m$ is often termed a constraint factor and is dependent upon the specimen geometry and material flow properties. Table 1 provides $m$-values for the three $a/W$ ratios and hardening exponents considered in the present work. Flow stress values for the power-law hardening model are again defined by Eq. (10). Linear regression is applied to plots of $J$ vs. $\sigma_{flow}\delta_t$ to obtain $m$ for each case. The geometry independent $m$-values for the SSY model also shown in Table 1 are obtained by simple conversion of the HRR $d_n$ values, which are found here to hold for the SSY models. The factors in Table 1 may be applied to express the axes of Figs. 10–12 in terms of $\delta_t$ rather than $J$.

| a/W | Strain–Hardening Exponent | | |
| --- | --- | --- | --- |
| | $n = 5$ | $n = 10$ | $n = 50$ |
| 0.05 | 1.78 | 1.50 | 1.30 |
| 0.15 | 1.85 | 1.57 | 1.45 |
| 0.50 | 2.04 | 1.79 | 1.69 |
| SSY | 2.10 | 1.71 | 1.37 |

*Table 1.* Constants '$m$' to Convert $J$ to CTOD, $\delta_t = J/(m\sigma_{flow})$, for Ramberg–Osgood Material Models

## DISCUSSION

Finite–element analyses for the SENB specimens convincingly demonstrate the effects of in–plane plastic deformation on the amplitude of crack–tip stresses. The loss of constraint (stress triaxiality) caused by impinging of global plastic deformation on the crack tip lowers the local stresses in the SENB specimens relative to small–scale yield values, when the SENB and SSY fields are compared at the same $J$. The divergence of SENB and SSY stress fields is accelerated by decreasing the $a/W$ ratio and lowering the degree of strain–hardening. For $a/W = 0.05$ and 0.15, agreement with the SSY stress field is achieved only at very low levels of loading and vanishingly small crack–tip plastic zones. Consequently, cleavage fracture toughnesses obtained from shallow notch specimens in the transition region will exhibit a strong geometry dependence. Limits of the type in Eq. (1) to assure size independent $J_c$ values for shallow notches would be so severe as to be impractical. Further-

more, the analyses show that SENB specimens of very low hardening materials containing deep notches ($a/W = 0.5$) also exhibit some loss of constraint that influences the local stress field once large-scale plasticity is achieved, i.e., deformations imposed following development of a plastic hinge.

Principal stress contours near the crack tip for the SENB specimens are self-similar and closely match the shape of contours for the SSY solution, when distances from the crack tip are normalized using $r\sigma_o/J$ or $r/\delta_t$, i.e., the similarity length scales for SSY. Amplitudes of the SENB stresses, however, scale with $J$ in a geometry dependent way which is substantially different from that predicted by the geometry independent SSY model. These observations suggest a crack-tip field for the SENB specimens which separates the principal stresses into multiplicative functions in the same spirit as HRR, such that

$$\sigma_i^{SENB}(r, \theta) = h_i(a/W; a\sigma_o/J; n) \cdot \sigma_i^{SSY} \qquad i = 1, 2, 3 \qquad (12)$$

where the full SSY fields have the form

$$\sigma_{ij}^{SSY}(r, \theta) = \sigma_o \cdot \hat{\sigma}_{ij}(r\sigma_o/J; n; \theta) \qquad (13)$$

Both $h_i$ and $\hat{\sigma}_{ij}$ are dimensionless functions of their arguments. In the crack-tip region where the plastic component of strain greatly exceeds the elastic component, the $h_{2,3}$ functions are related through the von Mises equivalent stress to $h_1$, which can be determined from a finite-element analysis. The most relevant aspect of Eqs. (12,13) is the separation of SENB stresses into a geometry and material dependent amplitude (or constraint) function, $h_i$, which does not vary with $r$ and $\theta$. When the loading is sufficiently small that amplitudes of crack-tip fields for the SENB specimens approach those of SSY conditions, $h_i \rightarrow 1$. Moreover, $\sigma_{ij}^{SSY} \rightarrow \sigma_{ij}^{HRR}$ as $r \rightarrow 0$. Although closed-form expressions for $\hat{\sigma}_{ij}$ in Eq. (13) are not yet available, resolution appears feasible through additional analyses of the SSY model for a broader range of material parameters. The framework of Eqs. (12) and (13) represents a logical extension of Parks [20] recently proposed concept of organizing elastic-plastic crack-tip fields into "similar" classes of increasingly complex form which degenerate to HRR under appropriate restrictions.

The existence of crack-tip fields that follow the form of Eqs. (12-13) permits a relatively straightforward construction of the relationship between SENB and SSY stresses for a given material and geometry ($a$, $W$) as

$$\sigma_i^{SENB} = \sigma_i^{SSY} \cdot H_i(\frac{J_{SENB}}{J_{SSY}}) \qquad (14)$$

Finite-element analyses of the type presented in Section 4 for the SENB specimens provide estimates for the $H_i$ functions (the $H_1$ functions defined using stresses on the symmetry plane, for example, are represented by the curves plotted in Figs. 10-12).

The SENB stress fields presented in Section 4 as determined by the finite-element analyses are for idealized plane-strain conditions. When the specimen thickness is finite,

however, through–thickness constraint can be considerably less than plane–strain conditions. Three–dimensional analyses of SENB specimens with in–plane mesh refinement comparable to that used for the 2–D models in the present study are very rare due to the enormous computational expense. One such analysis, recently performed by Narishimhan and Rosakis [37], provides some insight regarding the thickness required to maintain nearly plane–strain conditions through the thickness. They analyzed a SENB specimen having $a/W = 0.4$ where the crack length and remaining ligament length, $b$, were three and six times the thickness, $B$, respectively; thus thickness was the governing dimension. Very low hardening, $n = 22$ was specified for their analysis. Figure 15, constructed from the Narishimhan and Rosakis results, shows the stress normal to the crack plane, relative to the mid–thickness value. Data for three load steps are plotted which correspond to $B\sigma_o/J$ ratios of 235, 103, and 26.3. The relative distance ahead of the crack tip for each case lies in the range of 2–4 $\delta_t$. At the lowest $J$–value, the opening mode stress is nearly constant through the thickness except very close to the free surface. At the intermediate load step, the stress remains relatively constant over the middle 40% of the thickness; while at the largest $J$–value, the stress decreases continuously from the mid–thickness value toward the free surface. Narishimhan and Rosakis also performed a 2–D plane–strain analysis of the SENB. The 3–D, crack–tip stresses at mid–thickness displayed very good agreement with the 2–D, plane–strain values for the two lower $J$–values shown in Fig. 15. Thus, the deeply notched SENB specimen seems to maintain nearly plane–strain constraint through a significant portion of the thickness for $B\sigma_o/J$ ratios at least into the 150–200 range.

By combining the plane–strain analyses of the present study with the 3–D analyses of Narishimhan and Rosakis, specimen size limits to assure geometry independent cleavage fracture can be established, at least for deeply notched specimens. Figure 16 shows $J_{SENB}/J_{SSY}$ ratios for the $a/W = 0.5$ configuration as determined by the finite–element analyses of Section 4. The curves become relatively flat and approach unity when the $a\sigma_{flow}/J$ ratio exceeds approximately 200, although the rate at which each curve approaches the SSY limit depends on the hardening exponent. Thus, the recommended size requirements for deeply notched specimens are:

$$B, b, a \geq \frac{200J_c}{\sigma_{flow}}$$

(15a)

or

$$B, b, a \geq 300\delta_c$$

(15b)

These requirements, which would also apply to deeply notched compact specimens, guarantee fracture toughness results that are nearly size independent, but only when cleavage occurs without significant stable crack growth. Eq. (15a) is eight times more severe than the size requirements in E813–87 but not nearly as severe as E399–83. Consider, for example, a material with $J_c = 200$ kPa m, $\sigma_{YS} = 450$ MPa, and $\sigma_{flow} = 500$ MPa. The minimum thickness required for a valid $K_{Ic}$ test is 570 mm (22.4 in), while a 10 mm (0.39 in) thick

specimen satisfies the E813–87 requirement. An 80 mm (3.15 in) thick specimen is required to satisfy Eq. (15a).

While the present work has focused on effects of the in-plane geometry on fracture toughness; the effect of thickness requires considerably more study, especially the interaction of small $a/W$ ratios and thickness. Figure 15 shows that deeply notched test specimens can maintain nearly plane-strain conditions at mid-thickness to relatively high $J$-values, but the size of the plane-strain region decreases with plasticity. It should be possible to define an effective thickness, which equals the actual thickness for small-scale yielding, but which decreases with $J$ for large-scale yielding.

The effect of prior ductile crack growth also requires further study. The results presented here apply strictly to stationary cracks. Ductile crack growth affects cleavage toughness in at least two ways: (1) the stress fields ahead of a growing crack differ from those of a stationary crack; and (2) the growing crack samples more material which increases the likelihood of encountering a microstructural feature that triggers cleavage. Nevertheless, it seems reasonable, at least for a first-approximation, to correct cleavage fracture values for constraint loss using the results of Figs. 10–12 provided the amount of ductile growth is less than the size of the finitely deformed blunting zone, i.e., $\Delta a < \approx 2\delta_t$.

## SUMMARY AND CONCLUSIONS

Very detailed finite-element analyses for shallow and deeply notched SENB specimens have supported the development of a framework to quantify the effects of constraint loss due to in-plane plastic deformation on cleavage fracture toughness. The numerical results provide the relationship between $J$ and crack-tip stress fields when the specimen geometry and extent of plasticity invalidate the asymptotic HRR and small-scale yielding (SSY) solutions. Spatial variations of crack-tip stresses for the SENB specimens closely match those for the small-scale yielding model of crack-tip behavior, when distances from the crack tip are normalized as $r\sigma_o/J$. However, amplitudes of the SENB stress fields vary with $J$ in a substantially different manner than for small-scale yielding. Similar to the form of the HRR solutions, these results suggest a separation of the crack-tip stresses into an amplitude (or constraint) function which multiplies the SSY fields, where the material and geometry dependent amplitude term is determined through finite-element analyses of the type performed in this study. Consequently, the relationship between SENB and SSY crack-tip stresses can be expressed simply through functions of the $J_{SENB}/J_{SSY}$ ratios for a given material. Graphical forms of these functions are derived from the finite-element solutions and when applied to an A36 steel are shown to eliminate size effects on cleavage toughness data in the transition region. Moreover, the large scatter in toughness values inherent in experimental testing is significantly diminished through the constraint correction process.

The numerical results also demonstrate that crack-tip stresses for deeply notched SENB specimens with some strain-hardening closely approach small-scale yielding con-

ditions. Fracture toughness data obtained under such conditions should be independent of specimen geometry. To assure $J$ controlled cleavage fracture in deeply notched bend specimens, the results of this study indicate that all relevant dimensions of a specimen should exceed 200 $J_c/\sigma_{flow}$. This requirement is eight times more strict that current standards for $J_{Ic}$ testing but substantially less strict than requirements for $K_{Ic}$ testing.
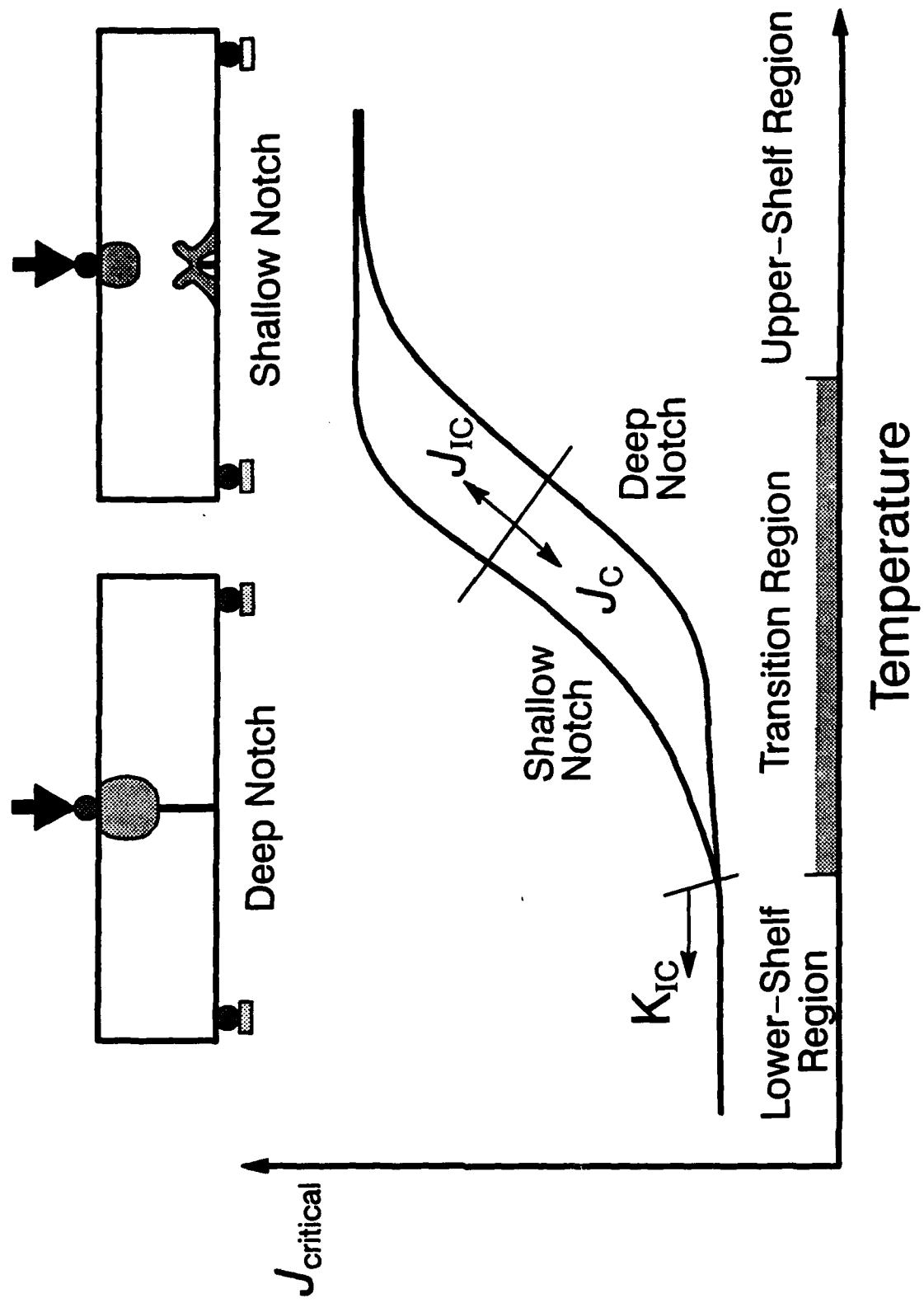
*Fig. 1.* Schematic *J*-temperature transition curve for shallow and deeply notched SENB specimens. Typical extents of plastic zones are shown for shallow and deeply notched specimens.

18
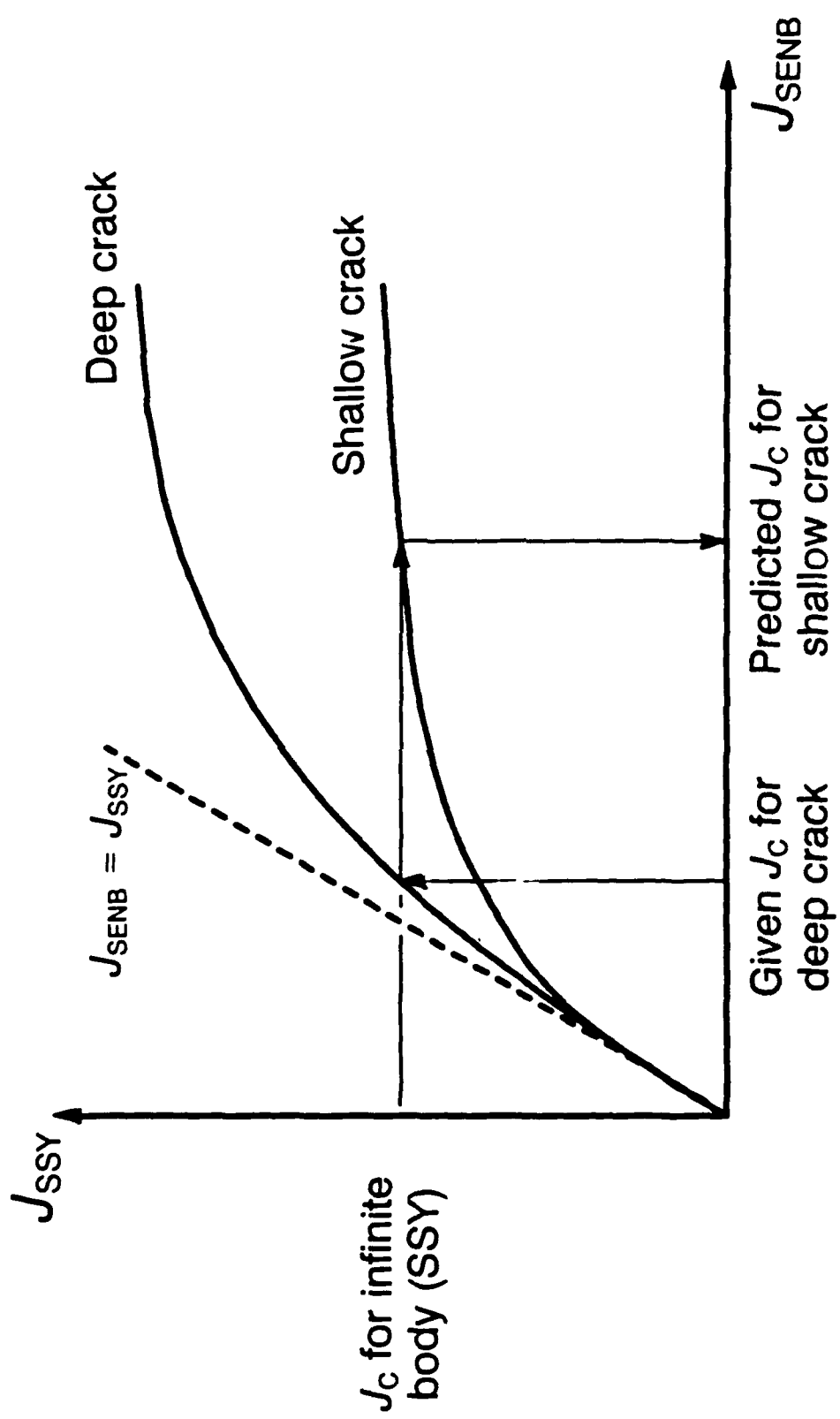
*Fig. 2.* Schematic of relationship between the *J*-integral values in SENB specimens for deep and shallow cracks with those of SSY conditions which generate equivalent opening mode stresses ahead of the crack tip.

19
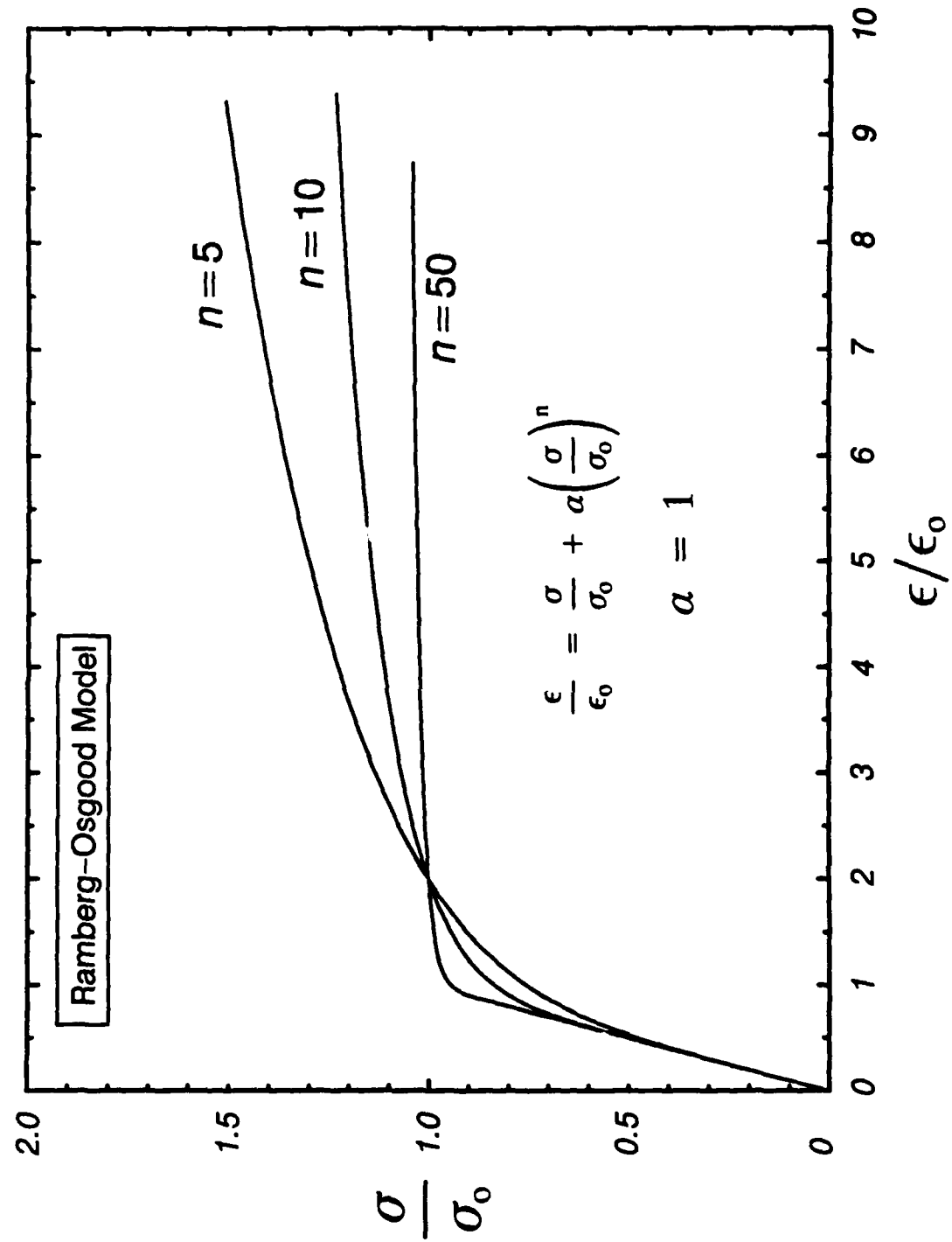
*Fig. 3.* Ramberg–Osgood stress–strain curves employed in the finite–element analyses.

$K_I$ Displacement Field
Imposed on Boundary

(Typ)

(720 elements, 2277 nodes)
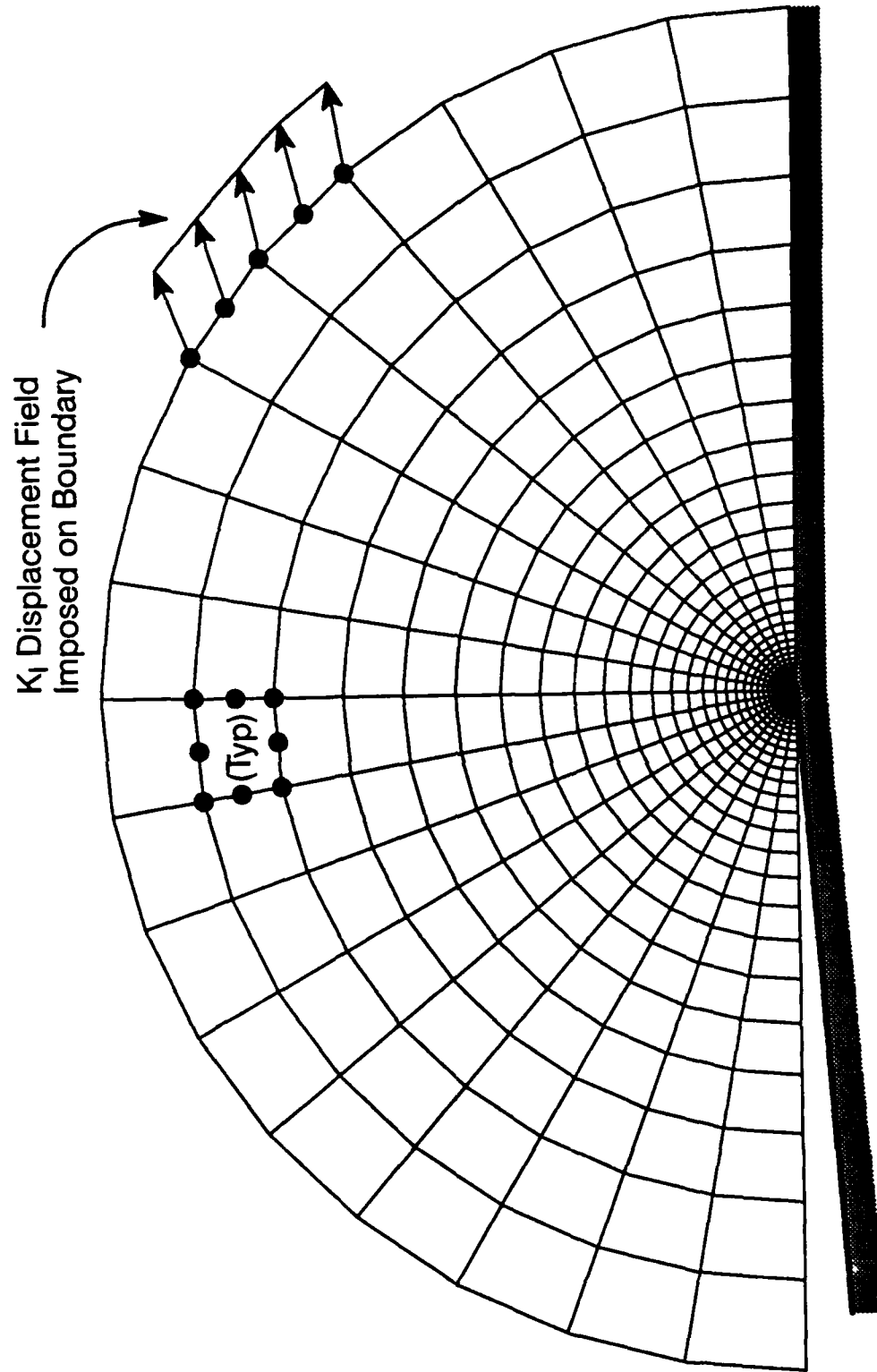
*Fig. 4.* Finite-element mesh for the small-scale yielding computations.

(Typ)

(350 elements, 1200 nodes for 1/2 symmetric model)
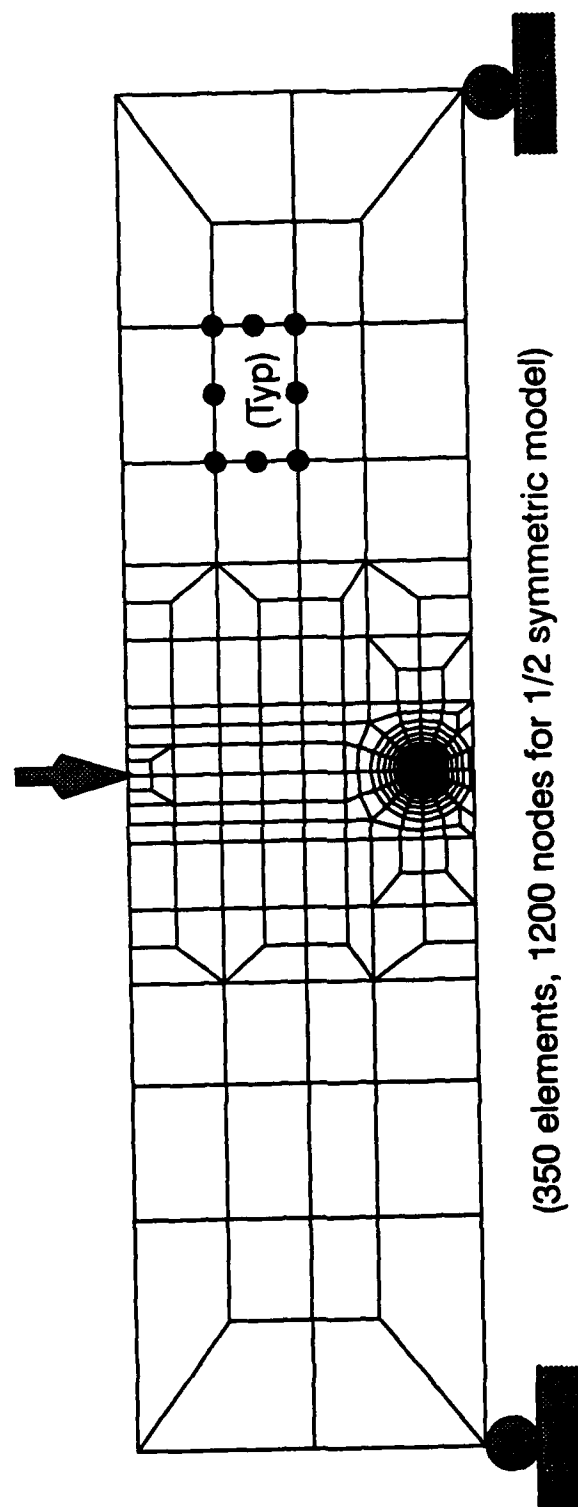
*Fig 5.* Typical finite–element mesh for plane strain analyses of the SENB specimens.
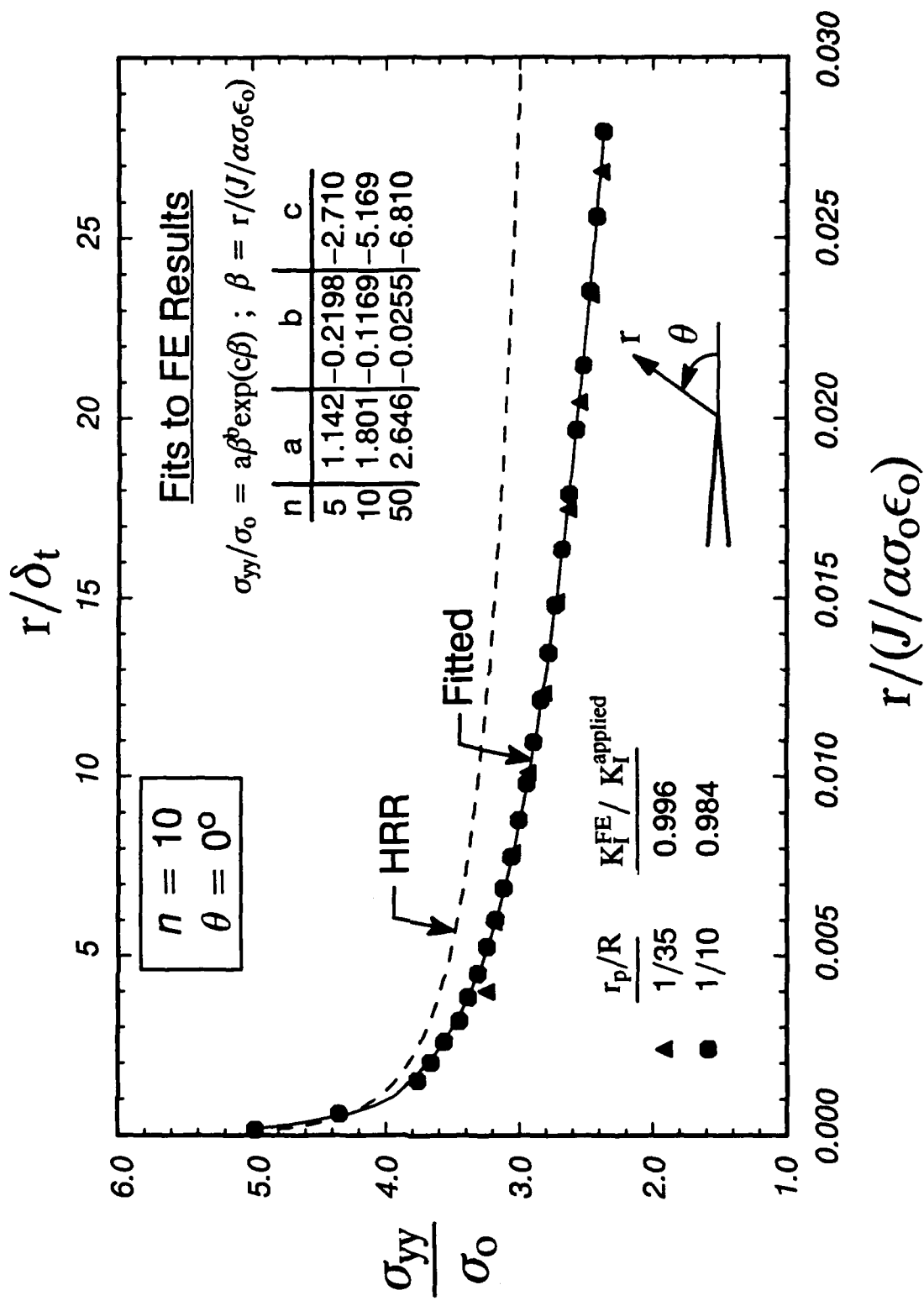
*Fig. 6.* Comparison of normalized crack opening stress in plane strain small–scale yielding *vs.* HRR solution for hardening exponent $n = 10$ at two levels of loading. Table of curve fitting parameters for small–scale yielding response for hardening exponents $n = 5, 10,$ and 50.
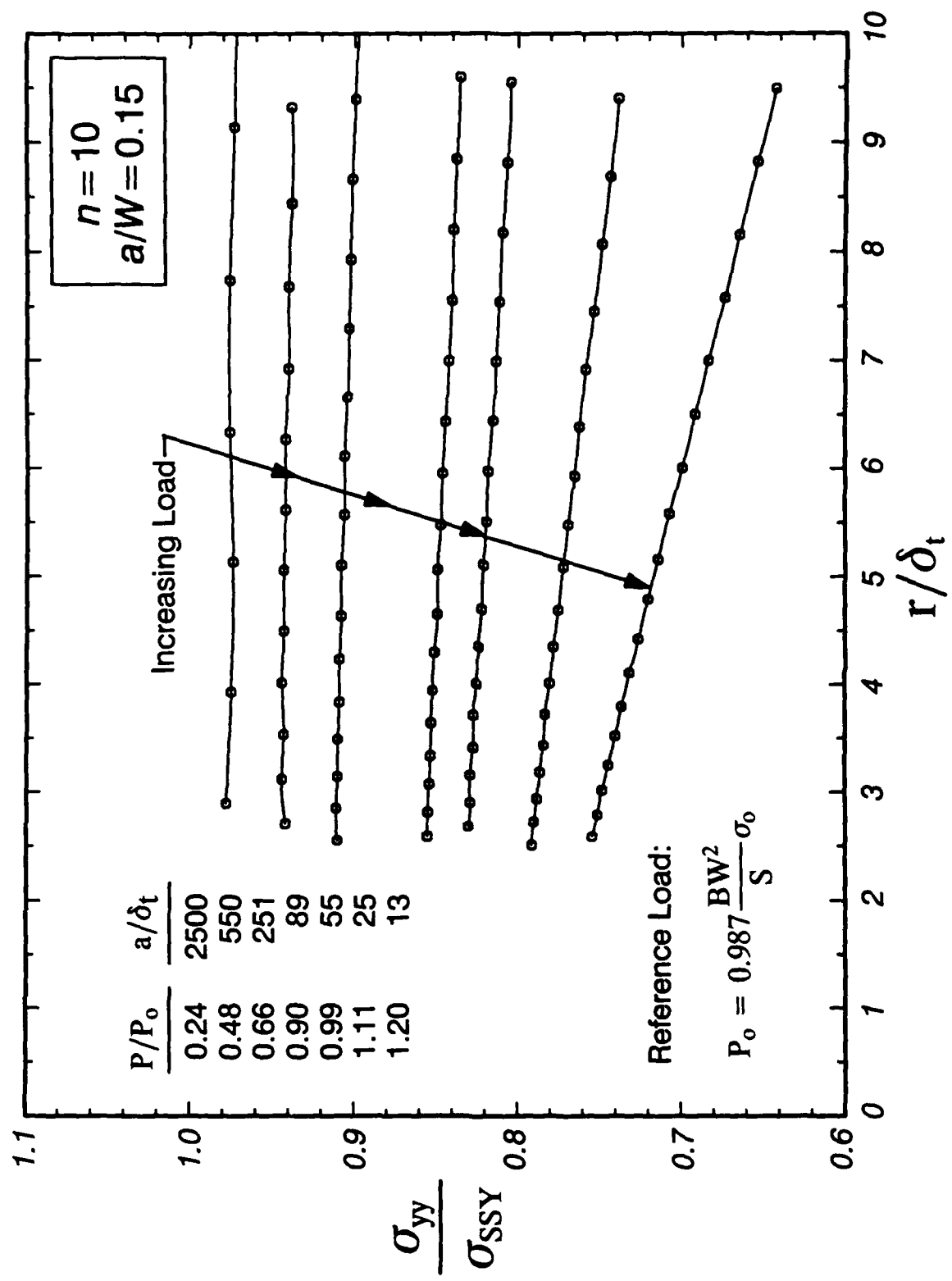
*Fig. 7.* Crack opening stress in SENB specimen normalized by the small–scale yielding stress at same applied *J*–value *vs.* normalized distance ahead of crack tip for increasing levels of applied load (hardening exponent *n* = 10, *a/W* = 0.15).
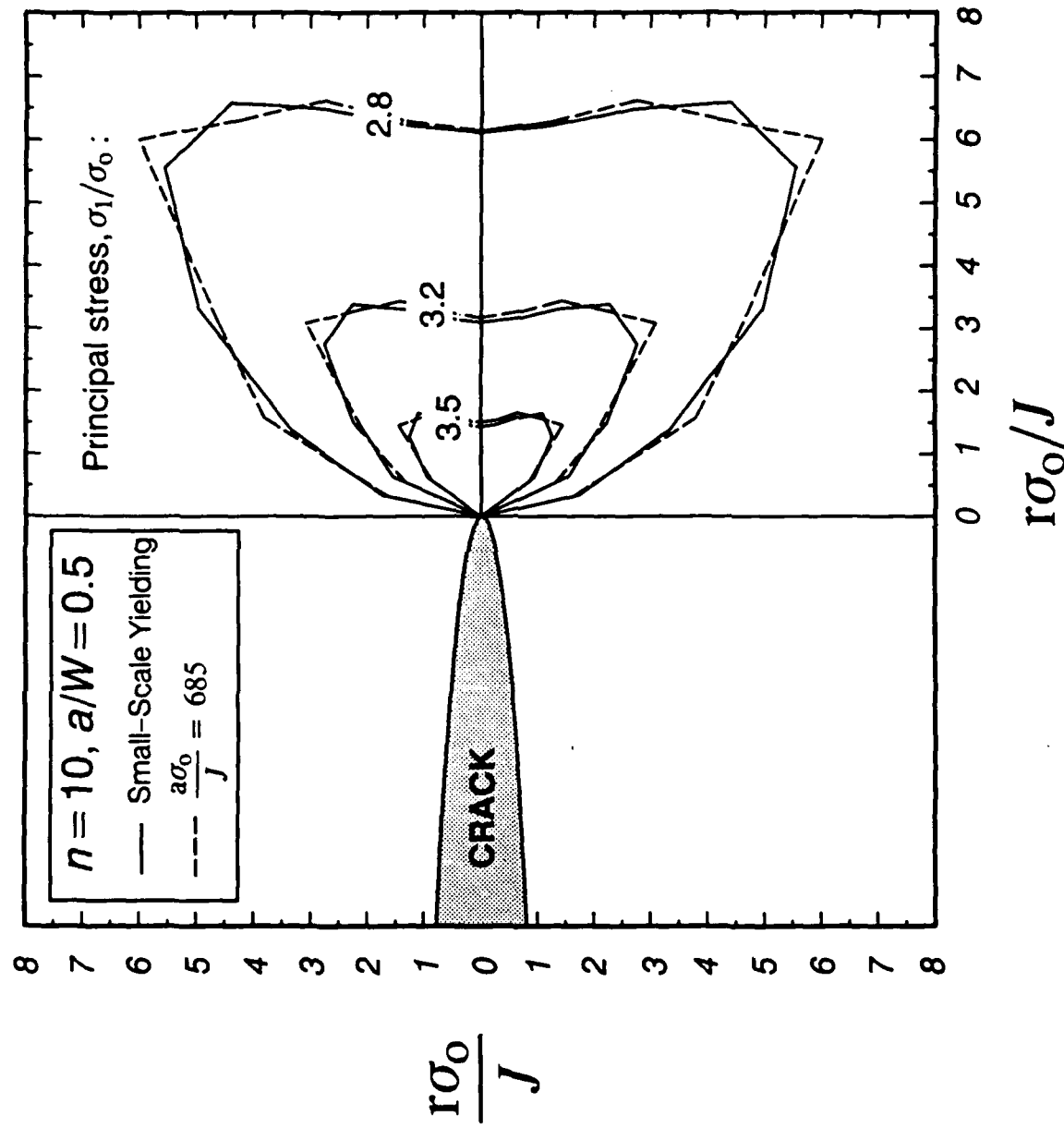
*Fig. 8.* Comparison of principal stress contours in small-scale yielding and in a SENB specimen for *a/W* = 0.5, hardening exponent *n* = 10.

*Fig 9.* Comparison of shapes for contours of principal stress for increasing levels of applied loading for hardening exponent *n* = 10, (a) very shallow crack, *a*/*W* = 0.05, (b) deep notch *a*/*W* = 0.5.
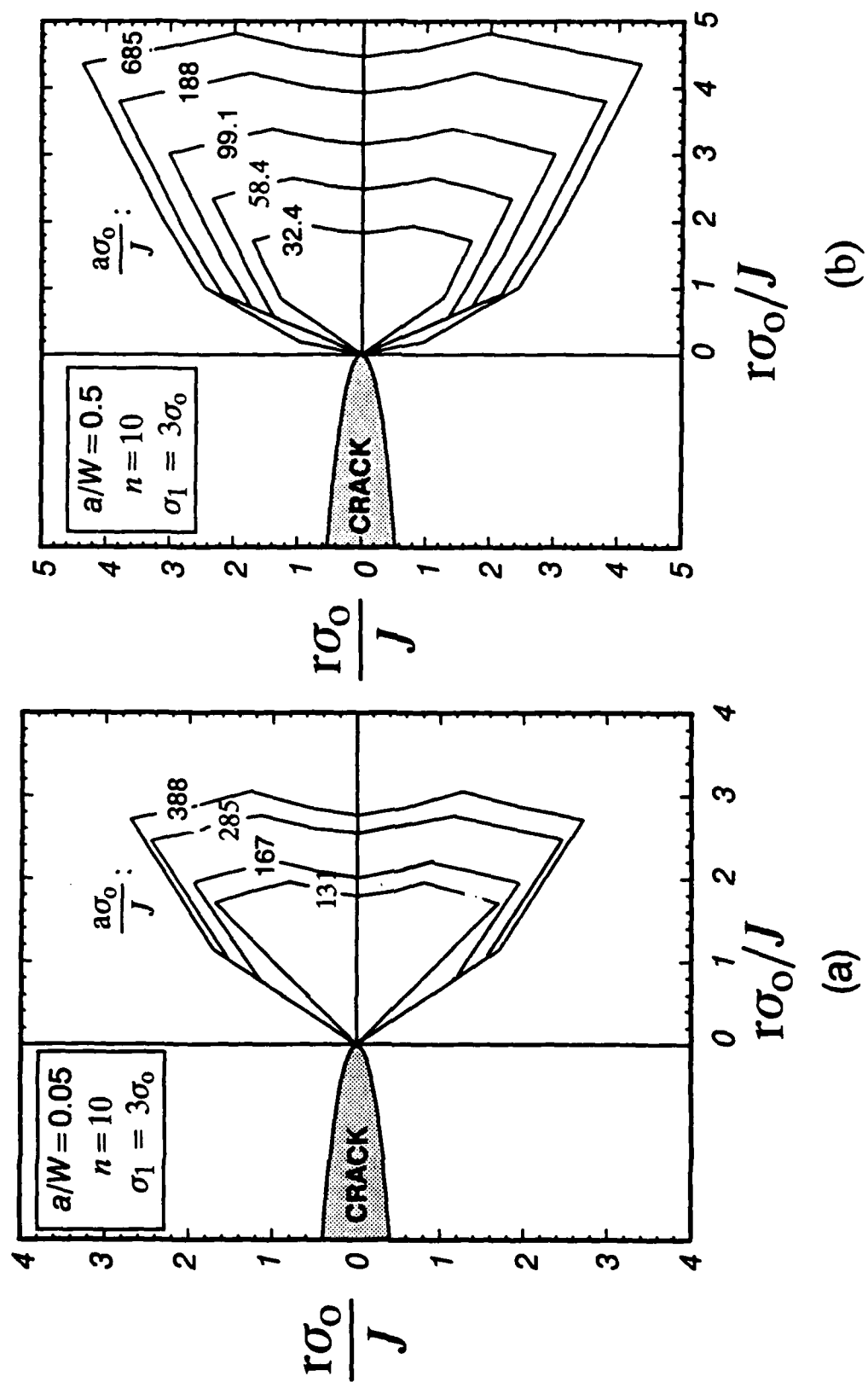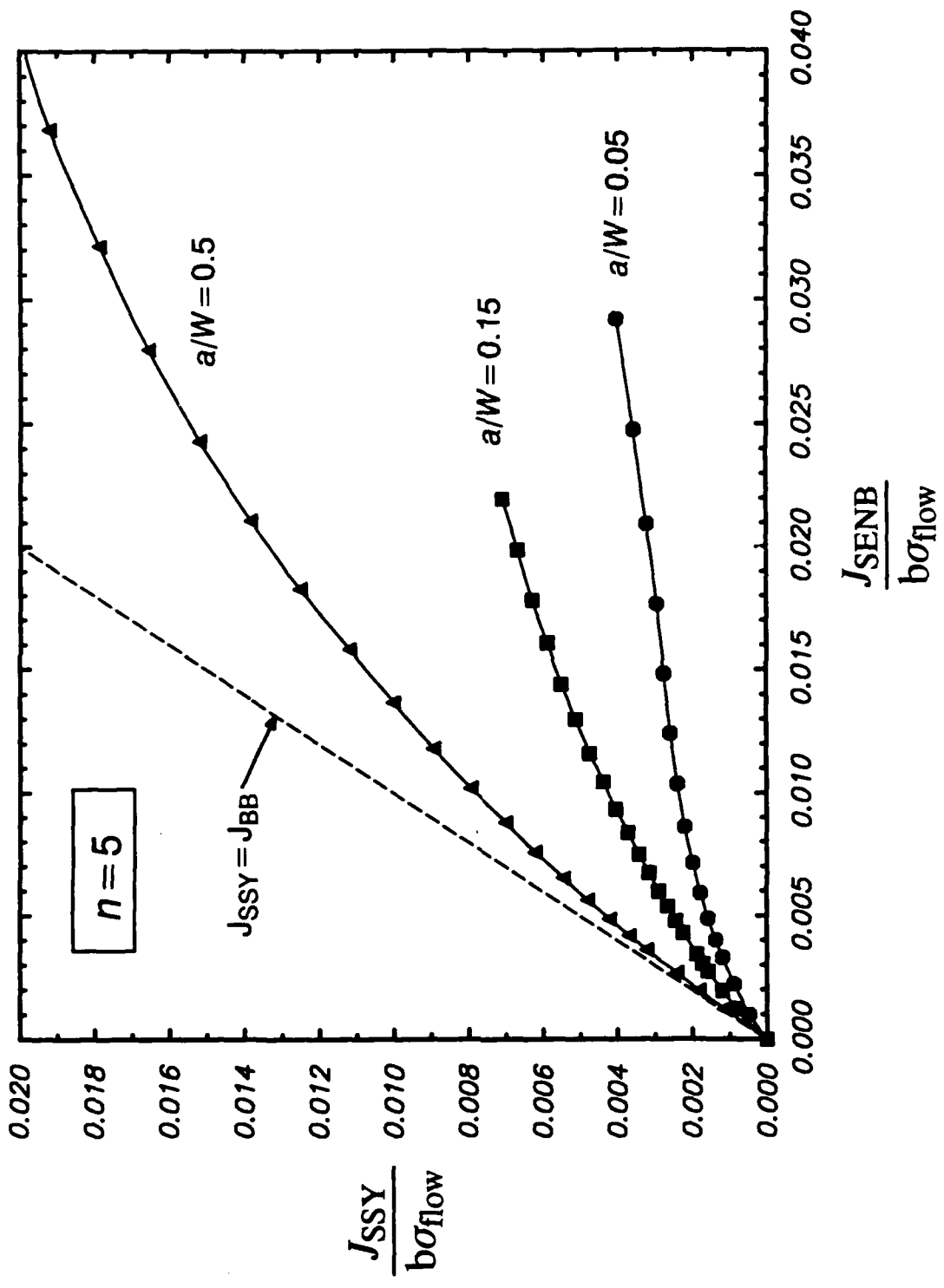
*Fig. 10.* Relationship between the normalized *J*-integral values in SENB specimens with those of SSY conditions which generate equivalent opening mode stresses ahead of the crack tip for hardening exponent *n* = 5.
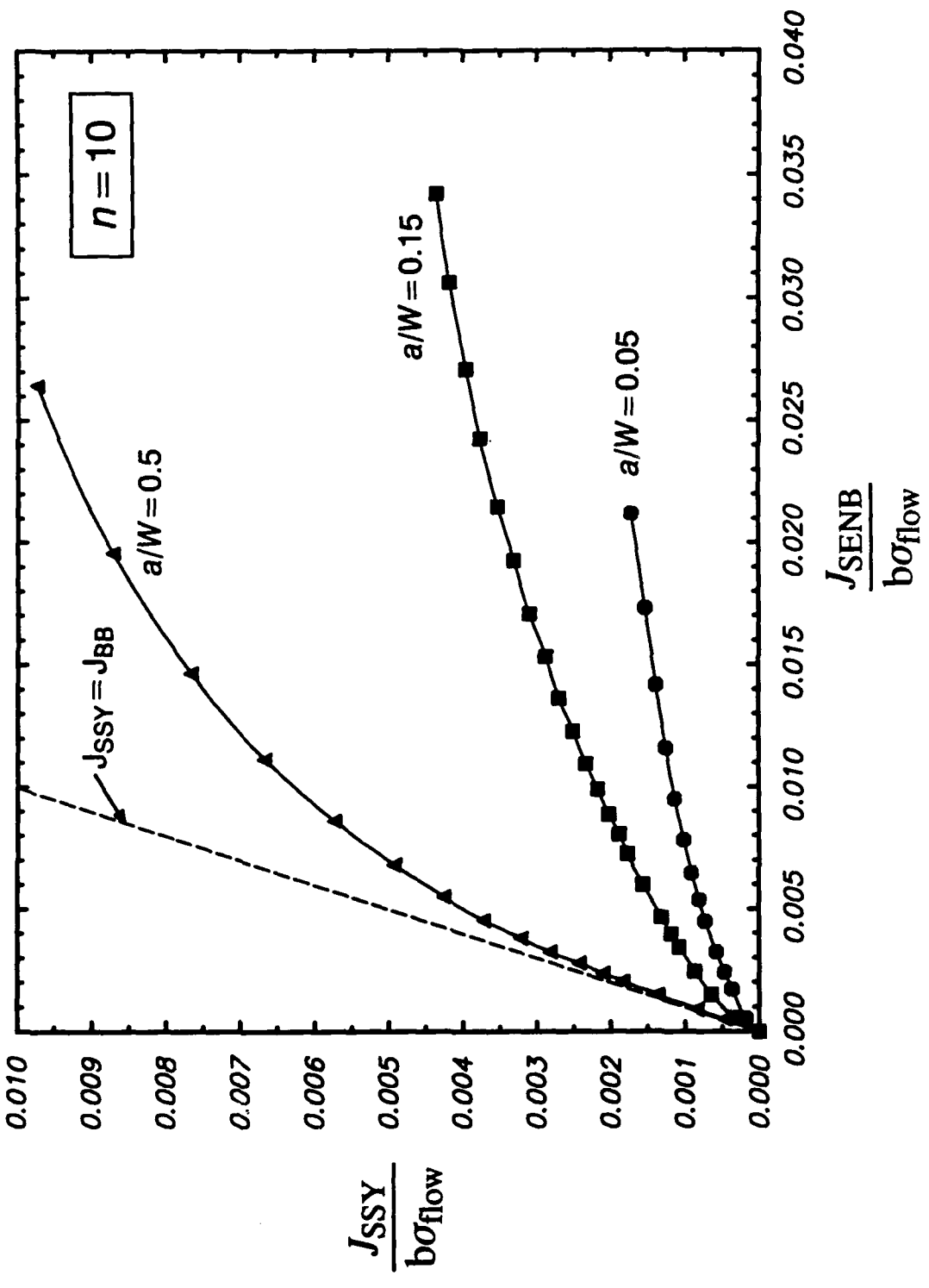
*Fig. 11.* Relationship between the normalized $J$-integral values in SENB specimens with those of SSY conditions which generate equivalent opening mode stresses ahead of the crack tip for hardening exponent $n = 10$.
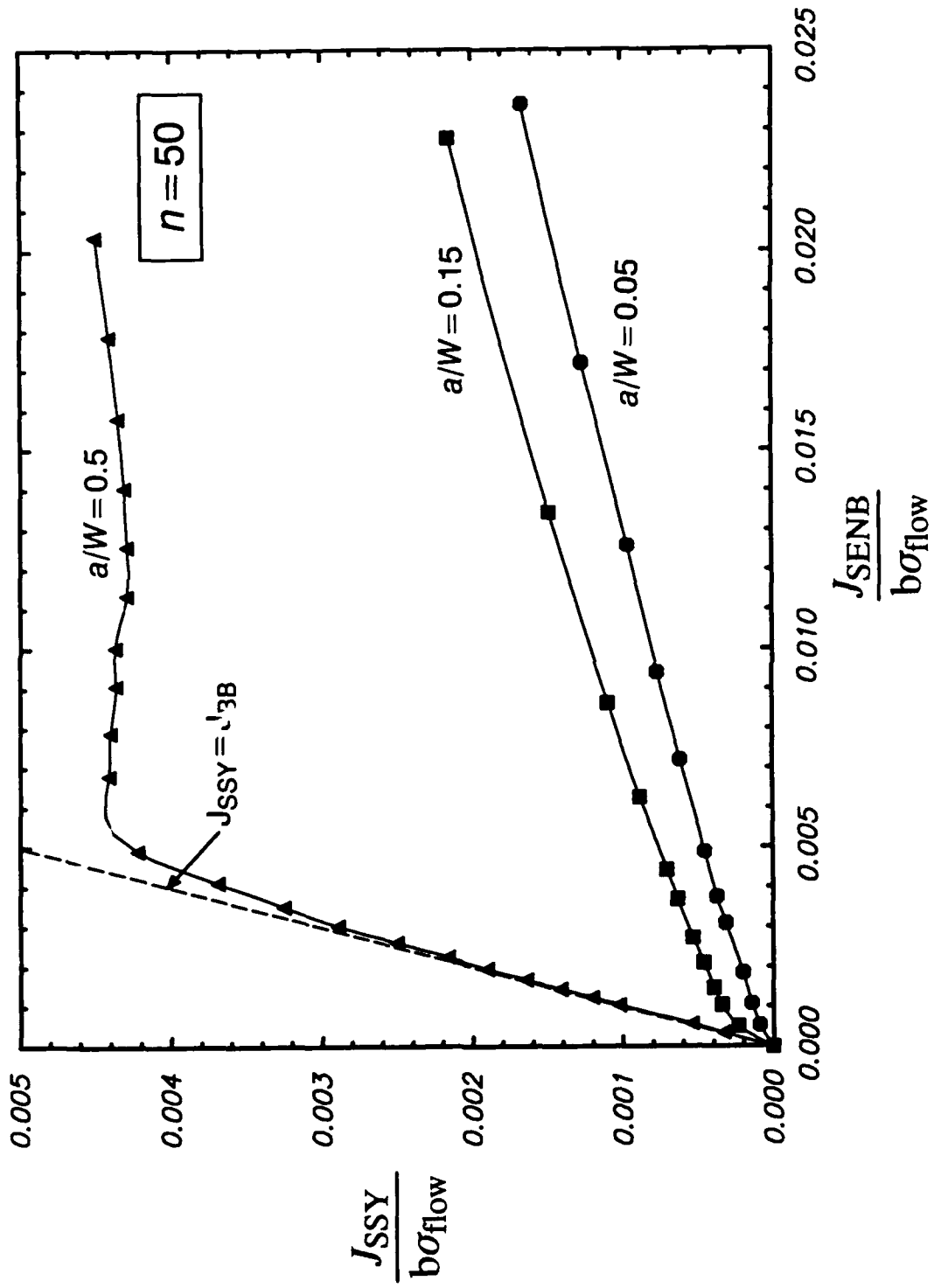
*Fig. 12.* Relationship between the normalized *J*-integral values in SENB specimens with those of SSY conditions which generate equivalent opening mode stresses ahead of the crack tip for hardening exponent *n* = 50.
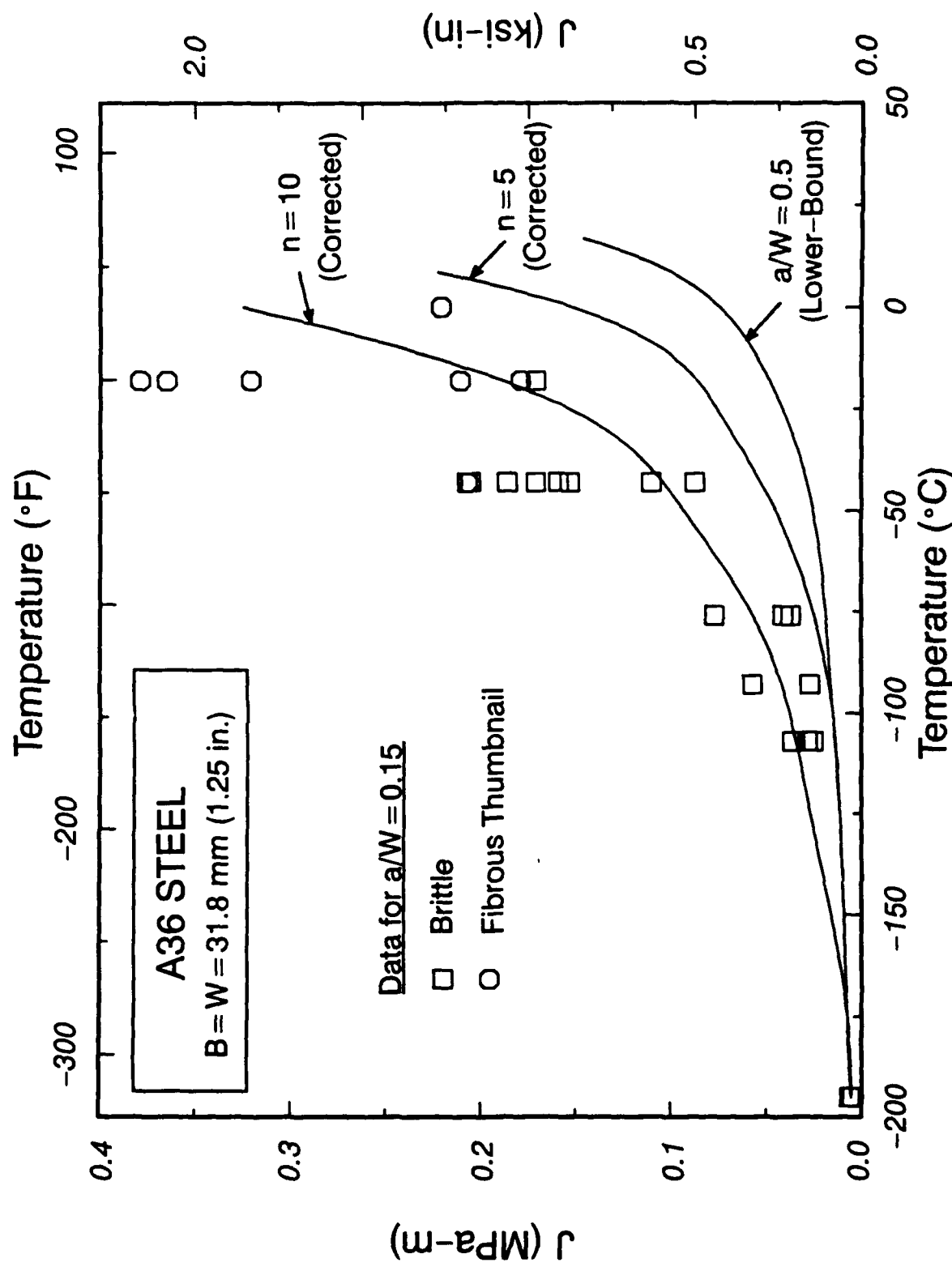
*Fig 13.* Experimentally determined critical *J*-values for an A36 steel showing the estimated lower–bound curves for *a/W* = 0.15 generated from the *a/W* = 0.5 curve using the constraint loss correction procedure.
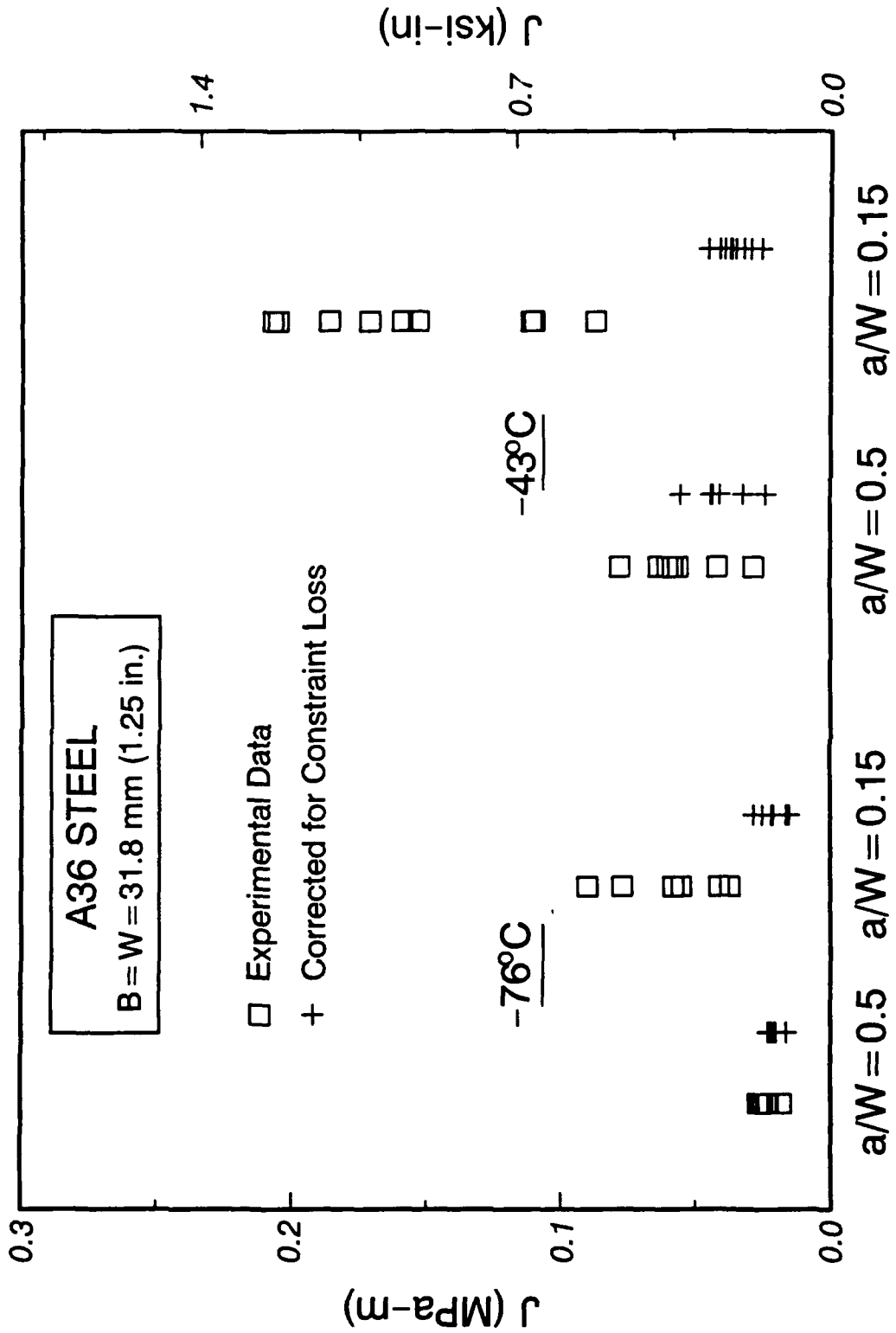
*Fig. 14.* Comparison of experimentally determined critical *J*-values for an A36 steel with data values corrected for constraint loss.

$$\frac{\sigma_{yy}}{\sigma_{yy}(z = 0)}$$
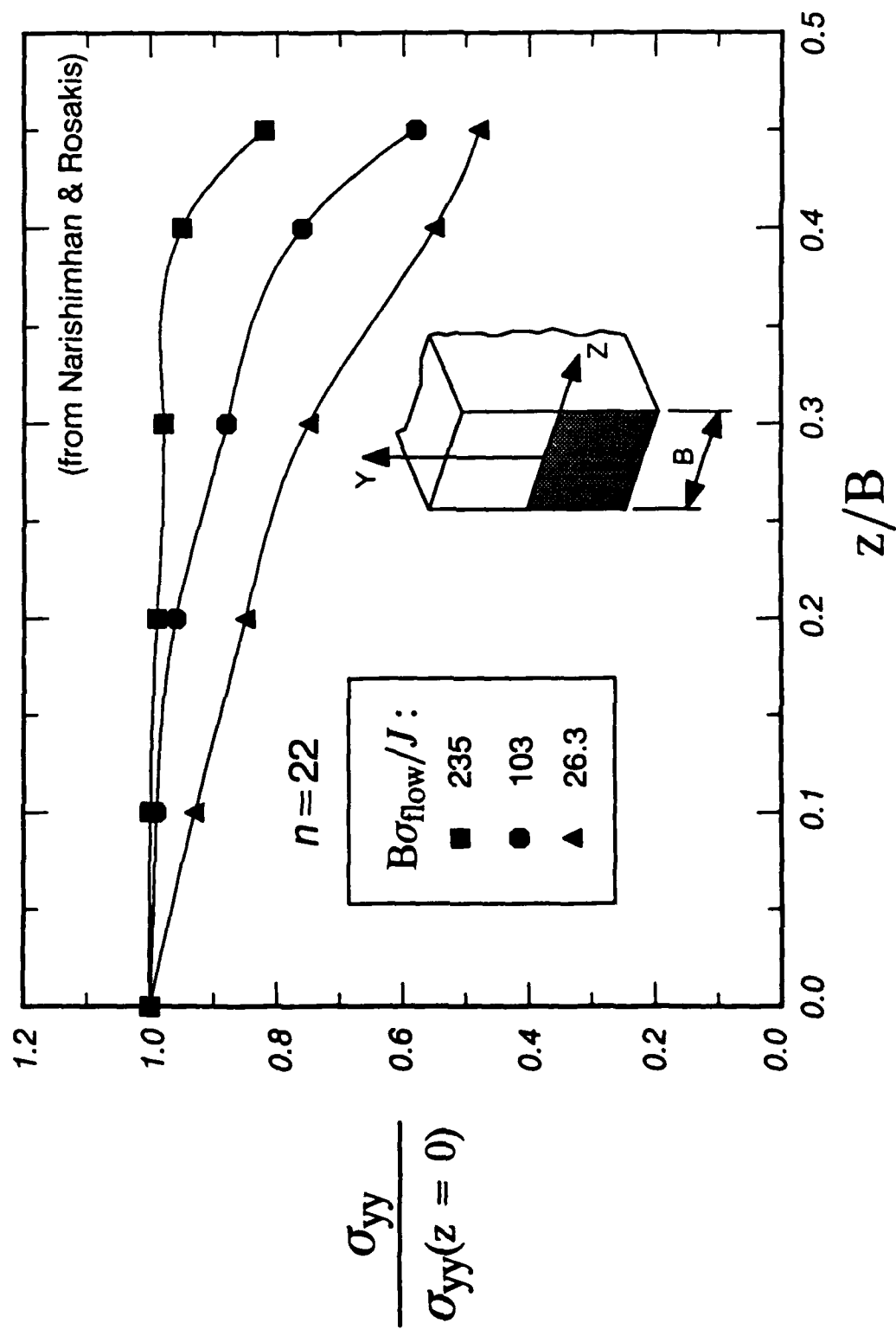
*Fig 15.* Comparison of crack opening stress through the thickness of a deeply notched SENB specimen relative to centerplane values.

32
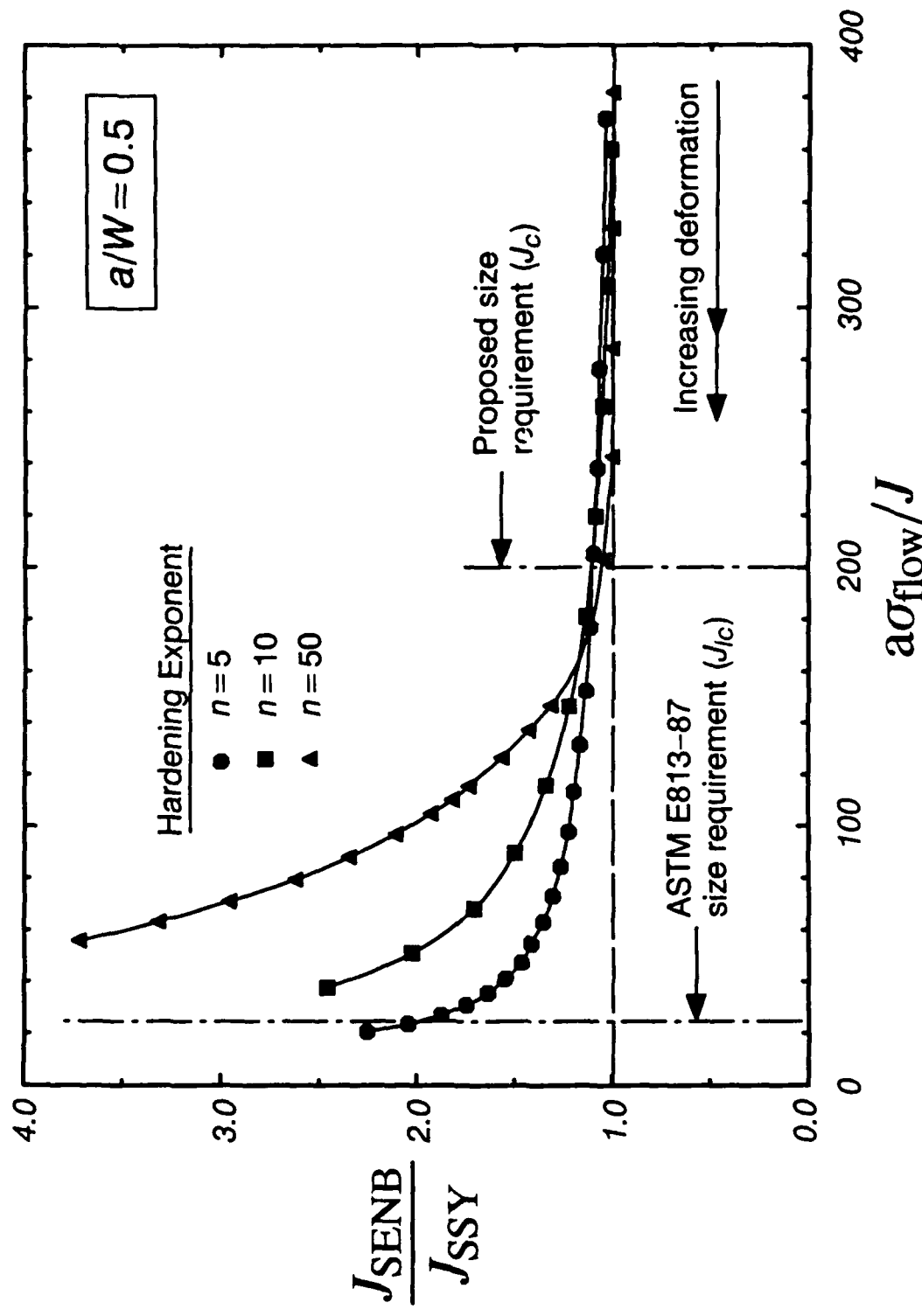
Fig. 16. Ratio of J-values in deeply notched, SENB specimens to J-values in small-scale yielding that generate the same crack opening stresses for increased levels of applied loading and hardening exponents $n = 5$, 10, and 50. Proposed size requirement for $J_c$ testing to assure geometry independent toughness measures and current size requirement for $J_{Ic}$ are indicated.

33

# REFERENCES

1. SOREM, W.A., DODDS, JR., R.H., and ROLFE, S.T. – The Effect of Crack Depth on Elastic–Plastic Fracture Toughness in Bend–Bar Specimens. *Structural Engineering and Engineering Materials*, SL Report 89-1, The University of Kansas Center for Research, Inc., 1989.

2. MATSOUKAS, G., COTTERELL, B., and MAI, Y.W. – Hydrostatic Stress and Crack Opening Displacement in Three–Point Bend Specimens with Shallow Cracks. *Journal of the Mechanics and Physics of Solids*, Vol. 34, No. 5, pp. 499–510, 1986.

3. DE CASTRO, P. M., SPURRIER, J. and HANCOCK, P. – An Experimental Study of the Crack Length/Specimen Width (a/W) Ratio Dependence on the Crack Opening Displacement (COD) Test Using Small–scale Specimens. *ASTM STP 677*, American Society for Testing and Materials, pp 486–497, 1979.

4. SUMPTER, J.D.G. – The Effect of Notch Depth and Orientation on the Fracture Toughness of Multi–pass Weldments. *International Journal of Pressure Vessel and Piping*, Vol. 10, pp. 169–180, 1982.

5. COTTERELL, B., LI, Q.F., ZHANG, D.Z., and MAI, Y.W. – On the Effect of Plastic Constraint on Ductile Tearing in a Structural Steel. *Engineering Fracture Mechanics*, Vol. 21, No. 2, pp. 239–244, 1985.

6. LI, Q.F. – A Study About $J_{Ic}$ and $\delta_i$ in Three–point Bend Specimens with Deep and Shallow Notches. *Engineering Fracture Mechanics*, Vol. 22, No. 1, pp. 9–15, 1985.

7. LI, Q.F., ZHOU, L., and LI, S. – The Effect of a/W Ratio on Crack Initiation Values of COD and J–integral. *Engineering Fracture Mechanics*, Vol. 23, No. 5, pp. 925–928, 1986.

8. ZHANG, D.Z., and WANG, H. – On the Effect of the Ratio a/W on the Values of $\delta_i$ and $J_{Ic}$ in a Structural Steel. *Engineering Fracture Mechanics*, Vol. 26, No. 2, pp. 247–250, 1987.

9. SUMPTER, J.D.G. – $J_c$ Determination for Shallow Notch Welded Bend Specimens. *Fatigue and Fracture of Engineering Materials and Structures*, Vol. 10, No. 6, pp. 479–493, 1987.

10. RICE, J.R. – A Path Independent Integral and the Approximate Analysis of Strain Concentrations by Notches and Cracks. *Journal of Applied Mechanics*, Vol. 35, pp. 379–386, 1968.

11. RICE, J.R., and JOHNSON, M.A. – in *Inelastic Behavior of Solids*, M.F. Kanninen et al., Eds., McGraw–Hill, New York, pp. 641–670, 1970.

12. RITCHIE, R.O., KNOTT, J.F., and RICE, J.R. – On the Relationship Between Critical Tensile Stress and Fracture Toughness in Mild Steel. *Journal of the Mechanics and Physics of Solids*, Vol. 21, pp. 395–410, 1973.

13. LIN, T., EVANS, A.G., and RITCHIE, R.O. – Statistical Model of Brittle Fracture by Transgranular Cleavage. *Journal of the Mechanics and Physics of Solids*, Vol. 34, pp. 477–496, 1986.

14. HUTCHINSON, J.W. – Singular Behavior at the End of a Tensile Crack in a Hardening Material. *Journal of the Mechanics and Physics of Solids*, Vol. 16, pp. 13–31, 1968.

15. RICE, J.R., and ROSENGREN, G.F. – Plane Strain Deformation Near a Crack Tip in a Power Law Hardening Material. *Journal of the Mechanics and Physics of Solids*, Vol. 16, pp. 1–12, 1968.

16. MCMEEKING R.M., and PARKS, D.M. – On the Criteria for *J*–Dominance of Crack–Tip Fields in Large–Scale Yielding. *Elastic–Plastic Fracture, ASTM STP 668*, American Society for Testing and Materials, pp. 175–194, 1979.

17. SHIH, C.F., and GERMAN, M.D. – Requirements for a One Parameter Characterization of Crack Tip Fields by the HRR Singularity. *International Journal of Fracture*, Vol. 17, pp. 27–43, 1981.

18. SHIH, C.F. – *J*–Dominance Under Plane Strain Fully Plastic Conditions: the Edge Crack Panel Subject to Combined Tension and Bending. *International Journal of Fracture*, Vol. 29, pp. 73–84, 1985.

19. PARKS, D.M., and YANG, Y.Y. – Elastic–Plastic Analysis of Part–Through Surface Cracks. In *Analytical, Numerical, and Experimental Aspects of Three Dimensional Fracture Processes*, ASME/SES, pp. 19–32, 1988.

20. PARKS, D.M. – Three–Dimensional Aspects of HRR Dominance. to appear in *Proceedings*, EGF Conference on Elastic–Plastic Fracture, Freiburg, October 1989.

21. ANDERSON, T.L., and WILLIAMS, S. – Assessing the Dominant Mechanism for Size Effects in the Brittle–to–Ductile Transition Region. *ASTM STP 905*, American Society for Testing and Materials, pp. 715–740, 1986.

22. ANDERSON, T.L., and STIENSTRA, D. – A Model to Predict the Sources and Magnitude of Scatter in Toughness Data in the Transition Region, *Journal of Testing and Evaluation*, Vol. 17, pp. 46–53, 1989.

23. SOREM, W.A., DODDS, JR., R.H., and ROLFE, S.T. – An Analytical and Experimental Comparison of Rectangular and Square CTOD Fracture Specimens of an A36 Steel. *Nonlinear Fracture Mechanics: Volume II – Elastic–Plastic Fracture, ASTM STP 995*, American Society for Testing and Materials, pp 470–494, 1989.

24. SHIH, C.F. – Tables of Hutchinson–Rice–Rosengren Singular Field Quantities. Brown University Report, MRL E–147.

25. SHIH, C.F. – Relationships Between the *J*–Integral and the Crack Opening Displacement for Stationary and Extending Cracks. *Journal of the Mechanics and Physics of Solids*, Vol. 29, pp. 305–326, 1981.

26. RICE, J.R., and TRACEY, D.M. – Computational Fracture Mechanics, in *Numerical and Computer Methods in Structural Mechanics,* eds. S.J. Fenves, et al., Academic Press, New York, pp. 585–623, 1968.

27. MCMEEKING, R.M. – Finite Deformation Analysis of Crack–Tip Opening Elastic–Plastic Materials and Implications for Fracture. *Journal of the Mechanics and Physics of Solids,* Vol. 25, pp. 357–381, 1977.

28. ANDERSON, T.L., and DODDS, JR., R.H. – Specimen Size Requirements for Fracture Toughness Testing in the Transition Region. Submitted to *Journal of Testing and Evaluation.*

29. DE LORENZI, H.G. and SHIH, C.F. – 3–D Elastic–Plastic Investigation of Fracture Parameters in Side–Grooved Compact Specimen. *International Journal of Fracture,* Vol. 21, pp. 195–220, 1983.

30. DODDS, JR., R.H. – Effects of Reduced Integration on the 2–D Quadratic Isoparametric Element in Plane Strain Plasticity. *International Journal of Fracture,* Vol. 19, pp. R75–R82, 1982.

31. BARLOW, J. – Optimal Stress Locations in Finite Elements. *International Journal for Numerical Methods in Engineering,* Vol. 10, pp. 243–251, 1976.

32. LI, F.Z., SHIH, C.F., and NEEDLEMAN, A. – A Comparison of Methods for Calculating Energy Release Rates. *Engineering Fracture Mechanics,* Vol. 21, pp. 405–421, 1985.

33. SHIH, C.F., MORAN, B., and NAKAMURA, T. – Energy Release Rate along a Three–Dimensional Crack Front in a Thermally Stressed Body. *International Journal of Fracture,* Vol. 30, pp. 79–102, 1986.

34. *PATRAN User's Manual,* Release 2.3. PDA Engineering, Inc., Costa Mesa, CA, 1989.

35. DODDS, R.H., and LOPEZ, L.A. – Software Virtual Machines for Development of Finite–Element Systems. *International Journal for Engineering with Computers,* Vol. 13, pp. 18–26, 1985.

36. HAIGH, J.R., and RICHARDS, C.E. – Yield Point Loads and Compliance Functions of Fracture Mechanics Specimens. CEGB Report RD/L/M461, 1974.

37. NARASIMHAN, R.., and ROSAKIS, A.J. – Three–Dimensional Effects Near a Crack Tip in a Ductile Three Point Bend Specimen – Part I: A Numerical Investigation. Report SM 88–6, California Institute of Technology, Division of Engineering and Applied Science, Pasadena, CA, 1988.

# INITIAL DISTRIBUTION

| OUTSIDE CENTER | CENTER DISTRIBUTION |
|---|---|

**OUTSIDE CENTER**

Copies
- 1   DDRE/LIB
- 1   CNO/OP98T
- 3   ONCR
  - 1 0225
  - 1 4325
  - 1 Library
- 15   NAVSEA
  - 1 SEA 05M
  - 1 SEA 05M2 (Mitchell)
  - 1 SEA 05R
  - 1 SEA 55Y2
  - 1 SEA 55Y23 (Nichols)
  - 1 SEA 55Y23 (Barbaro)
  - 1 SEA 55Y3
  - 1 SEA 55Y3 (Manuel)
  - 1 SEA 55Y3 (Sieve)
  - 1 SEA 55Y3 (Woods)
  - 1 SEA 55W3
  - 1 SEA 55W31
  - 1 SEA 55W31 (Robinson)
  - 2 SEA 99621
- 12   DTIC
- 1   NAVPGSCOL
- 1   USNROTCU
  NAVAMINU MIT
- 2   NRL
  - 1 Code 6380
  - 1 Code 6384

**CENTER DISTRIBUTION**

Copies

| Copies | Code | Name |
|---|---|---|
| 1 | 011 | |
| 1 | 011.5 | Caplan |
| 1 | 172 | Rockwell |
| 1 | 1720.4 | Wiggs |
| 1 | 1720.4 | Sickles |
| 1 | 1720.4 | Gifford |
| 1 | 173 | Beach |
| 1 | 174 | Hansen |
| 1 | 28 | Wacker |
| 1 | 2801 | Crisci |
| 1 | 2801 | Ventriglio |
| 1 | 2802 | Morton |
| 1 | 2803 | Cavallaro |
| 1 | 2809 | Malec |
| 3 | 281 | Gudas |
| 3 | 2814 | Montemarano |
| 20 | 2814 | Kirk |
| 1 | 2814 | Hackett |
| 1 | 2814 | R. Link |
| 1 | 2814 | Vassilaros |
| 1 | 2815 | Holsberg |
| 1 | 2815 | De Loach |
| 1 | 283 | Singerman |
| 1 | 284 | Fischer |
| 1 | 522.1 | TIC |
| 1 | 5231 | Office Services |